Title:
Temperature: a key driver of Earth's habitability over the last billion years

Authors:
Kristin D. Bergmann[1*], Nicholas Boekelheide[1], Julia W. Clarke[1], Marjorie D. Cantine[1,2], Julia Wilcots[1], Noah T. Anderson[1], Adam B. Jost[1], Olivia Laub[3,4], Juliana Drozd[1,5], Samuel L. Goldberg[1,6], Tyler Mackey[1,7], Fran Meyer[1,5], Athena Eyster[1,8]

[1]Department of Earth, Atmospheric and Planetary Sciences, Massachusetts Institute of Technology, Cambridge, MA 02139

[2]now at Institut für Geowissenschaften, Goethe-Universität, Frankfurt Frankfurt, Germany

[3]Department of Geology, Carleton College Northfield, MN 55057

[4]now at Geosciences Department, Utah State University Logan, UT 84322

[5]now at Department of Geosciences, Pennsylvania State University State College, PA 16801

[6]now at Rosenstiel School of Marine and Atmospheric Science, University of Miami Miami, FL 33149

[7]now at Department of Earth and Planetary Sciences, University of New Mexico Albuquerque, NM 87131

[8]now at Department of Geoscience, University of Wisconsin, Madison Madison, WI 53706

[*]To whom correspondence should be addressed; E-mail: kdberg@mit.edu.

The habitability and ecology of Earth is fundamentally shaped by surface tem-

perature, but the temperature history of our planet is not easily reconstructed, especially before the evolution of early biomineralizing animals. This work presents a billion-year-long, high-resolution, mineral-specific record of oxygen isotope measurements in shallow marine rocks. Clumped isotope paleothermometry results from four minerals resolves previous ambiguity in seawater oxygen isotope composition and confirms that long-term cooling punctuated by short-lived temperature extremes are dominant components of this record. We consider post-depositional effects by comparing Phanerozoic rock and fossil records, and identify temporal and spatial controls on alteration. Furthermore, this record is suggestive of key differences in dolomite ($CaMg(CO_3)_2$) formation processes between the Neoproterozoic (1000–538.8 Ma) and Phanerozoic (538.8–0 Ma), consistent with previous suggestions based on petrographic and sedimentological observations. This record, when viewed alongside the fossil record, suggests temperature change is tightly coupled to extinction and origination in the history of life and carbon cycle perturbations over the last billion years.

One sentence summary: Earth's long-term temperature evolution, as recorded by oxygen isotopes in shallow marine rocks, shows that temperature was a key variable in the expansion of complex life.

Uncertainty in Earth's surface temperature through time To understand why complex life evolved on Earth—and to grasp how rare it may be in the Universe—we must identify and quantify the variables that have controlled habitability and permitted the emergence of complex life. The temperature of Earth's surface environments is a key control on modern ecosystems, yet it is poorly constrained in Earth's distant past. Quantifying Earth's surface temperature

history in deep time ($\sim 10^9$ y) will inform our understanding of the interplay between climate, carbon, and life on Earth.

For decades, consensus from climate models and data analyses have held (*1–4*) that average global temperatures in the deep past were similar to those observed in the Cenozoic (*5*). Previous efforts document a protracted increase towards the modern in the oxygen isotopic composition (δ^{18}O) of various minerals precipitated from seawater that are preserved in ancient marine sedimentary rocks (e.g. calcite (*1, 2, 6*), apatite (*6, 7*), chert (*8, 9*), iron oxides (*3*)). However, interpretations of this increase in mineral δ^{18}O values are inherently equivocal the observed values depend on the temperature of precipitation, the oxygen isotopic composition of water, and post-depositional alteration. The ambiguity of long-term mineral δ^{18}O records has provoked a half-century of debate about the relative contributions of a long-term cooling trend (*7–9*), a secular increase in seawater δ^{18}O values (*1–4*), or the importance of post-depositional alteration (*10*).

Carbonate clumped isotope (Δ_{47}) thermometry has the potential to resolve this debate (*11*). The thermodynamic underpinning of clumped isotope thermometry relies on the temperature-dependence of multiple substitutions of heavy isotopes within a given carbonate molecule independent of seawater oxygen isotope composition (*11*). In the absence of post-depositional alteration, seawater δ^{18}O values can be calculated from coupled measurements of Δ_{47}-temperature and mineral δ^{18}O values (*11*). Paired with petrography and constraints on burial history, it also yields insights into post-depositional alteration and solid-state reordering (i.e., (*12–14*)).

To build an improved record of Earth's marine temperature history, we must quantify the competing effects of temperature and seawater oxygen isotope composition using clumped isotope thermometry, and also contend with significant changes in the carbonate record over its

3.8 billion year history. These changes include a lack of open ocean and deep ocean records before ∼145 Ma (*15*), coastal fossils prior to 538.8 Ma (*16*), and changes in the dominant primary carbonate mineralogy of skeletons and precipitates (*17*). Due to the fundamental limits of the carbonate rock record, a comprehensive, continuous carbonate oxygen isotope record will inevitably include samples that have been altered, that formed from environments with varying primary temperatures and water oxygen isotope values, and that reflect material-specific formation processes (*15, 18*). This paper presents a time-resolved compilation of limestone ($CaCO_3$) and dolomite ($CaMg(CO_3)_2$) δ^{18}O values spanning the last billion years. We contextualize this compilation with measurements of fossil δ^{18}O values (*5, 16*) and Δ_{47}-temperature and water $\delta^{18}O_{VSMOW}$ values derived from limestone, dolomite, and calcite, aragonite and apatite fossils (*12–14, 19–21*). After exploring controls on δ^{18}O and δ^{13}C values and variability between materials, we develop an approach to minimize the influence of alteration and present an side by side estimate of shallow marine temperature and δ^{13}C over the last billion years. Finally, we consider the implications of our results for Earth's habitability and the evolution of complex life.

Assessing temperature versus seawater oxygen isotope evolution over the last billion years

In total, our compilation includes 40,368 mineral δ^{18}O and 146 Δ_{47}-temperature values of marine limestone rocks and 15,688 mineral δ^{18}O and 230 Δ_{47}-temperature values of dolomite rocks (Fig. 1)(See SI for a complete reference list). This record is combined with 6,114 previously compiled mineral δ^{18}O values and 206 Δ_{47}-temperature measurements of calcite, aragonite, and apatite fossils (e.g., brachiopods and belemnites) from shallow nearshore environments and 7,647 δ^{18}O values from open ocean planktonic and 56,384 deep sea benthic foraminifera (*5, 12–14, 16, 19–21*). All datasets use a consistent age model in the Phanerozoic (*22*) and Neoproterozoic (*23–25*).

Initially, we consider all mineral δ^{18}O and Δ_{47}-temperature values in the compilation, despite clear evidence for alteration in some samples. We explore the implications of two end-member interpretations of the long-standing paleoclimate debate using the mineral-specific dependence of water oxygen isotopic composition and temperature on mineral δ^{18}O values (*26, 27*). In Scenario 1, we assume an invariant seawater $\delta^{18}O_{VSMOW}$ value of $-1.2‰$, an estimate of recent ice-free seawater δ^{18}O (*28, 29*), which we use to calculate the Gaussian kernel density estimate of temperature over time (*26, 27*)(Fig. 2, thin line, left panels). Within Scenario 1, we increase the seawater $\delta^{18}O_{VSMOW}$ value to -0.8 to $-0‰$during known glacial intervals to simulate ice volume (*6*), but this modification is distinctly different than the common hypothesis that seawater $\delta^{18}O_{VSMOW}$ was as light as $-6‰$during the earliest Phanerozoic and Precambrian (*1–3*) (*30*). In Scenario 2, we hold seawater temperature at a constant 25°C over the last billion years, and use mineral δ^{18}O values to calculate the Gaussian kernel density estimate of seawater δ^{18}O values (*26,27*)(Fig. 2, thin line, right panels). This scenario predicts seawater $\delta^{18}O_{VSMOW}$ values with a mode of $-6‰$ in the Neoproterozoic in line with previous suggested values (*1, 2*)(Fig. 2). Post-depositional alteration generally lowers mineral δ^{18}O—leading to a right-skewed distribution in Scenario 1 and a left-skewed distribution in Scenario 2 (Fig. 2, thin lines).

To resolve Scenarios 1 and 2, we overlay Δ_{47}-temperature and Δ_{47}-derived seawater δ^{18}O values from five different materials (limestone (n = 216) and dolomite rocks (n = 134); a collection of all calcite, apatite and aragonite fossils (n = 191)) (*12–14, 19–21*)(Fig. 2, bold lines). We opt to use a -temperature cutoff of $\leq$75°C to minimize the contributions from solid state reordering and deep burial diagenesis and maximize the contributions from primary and shallow marine diagentic environments. The portion of overlap (η) between Gaussian kernel density estimates between each scenario (light lines) and Δ_{47} results (bold lines), is shaded (Fig. 2).

There is significant overlap between Scenario 1 and the Δ_{47}-temperature population over the entire record. While there is overlap between Scenario 2 and Δ_{47}-derived water δ^{18}O values in the Phanerozoic fossil and limestone rock populations, there is little overlap with Scenario 2 in the Precambrian limestone and dolomite rock populations. Instead, the median of Δ_{47}-derived water δ^{18}O values indicate that shallowly buried carbonate rocks and fossils have lithified in the presence of fluids with $\delta^{18}O_{VSMOW}$ values similar to or greater than -1.2‰ for the last billion years (Fig. 2). Our Neoproterozoic results are compatible with an independent estimate of seawater $\delta^{18}O_{VSMOW}$ of -1.33 ± 0.98‰ from a Neoproterozoic ophiolite (*31*) and even older ophiolite δ^{18}O datasets (i.e., (*32, 33*)). Our results are inconsistent with interpretations for a more negative seawater δ^{18}O value based on iron oxide measurements from the Neoproterozoic, although iron oxide data is sparse through this interval (*3*).

Studies often document a range in Δ_{47}-temperatures from a given location and time interval, reflecting a combination of differential alteration and solid state reordering (*12–14, 19–21*)(right-skewed bold distributions in Fig. 2, Scenario 1). Outside of regions affected by solid state reordering, petrographic and crystallographic observations show that the preservation of primary carbonate fabric coincides with minimum Δ_{47}-temperatures and that visibly altered carbonates record elevated Δ_{47}-temperatures, suggesting that the lowest Δ_{47}-temperatures record marine or shallow burial conditions (*12–14, 19, 20, 34, 35*)(Fig. 2). Samples with elevated Δ_{47}-temperatures have apparent Δ_{47}-derived elevated seawater $\delta^{18}O_{VSMOW}$ values either reflecting sediment-buffered alteration or solid state reordering processes that do not reset mineral δ^{18}O values; this trend creates a right-skewed distribution (bold lines in Fig. 2, Scenario 2).

Time-dependent variability across materials We explore controls on variability in the δ^{18}O-derived temperature data in Scenario 1a constant seawater $\delta^{18}O_{VSMOW}$ value except during known glacial intervalsby considering limestone, dolomite, coastal shallow marine fossils, open

ocean planktonic foraminifera, and benthic foraminifera records individually and relative to each other both temporally and spatially (Fig. 3, Fig. S2, S3). There is agreement in both distribution and variance between limestone and coastal fossils for many time periods in the Phanerozoic Era, particularly in the early Phanerozoic (Fig. 3A,B, Fig. S3). The Late Paleozoic Ice Age (345–290 Ma) is one point of difference, likely because of the compounding effects of meteoric alteration on limestone from high amplitude sea level oscillation and a switch from calcite to aragonite as the dominant primary carbonate mineralogy (*36*)(Fig. 1,3). This is similar to what is observed from meteoric alteration associated with glacial-interglacial sea level oscillation in the Bahamas (*37*). In the Cenozoic as a whole, the bulk shallow marine limestone dataset is currently sparse as it is less common to report δ^{18}O values in publications—a sparse record can be more easily biased by alteration at one site(Fig. 3A,B).

Compiling all available mineralogies in our database reveals the 'dolomite problem', the significant contribution dolomite makes to the carbonate record in the Neoproterozoic and early Phanerozoic compared to its rarity in the recent (Fig. 1). Intriguingly, the Neoproterozoic limestone and dolomite records maintain a δ^{18}O fractionation offset consistent with equilibrium precipitation from the same temperature and fluid $\delta^{18}O_{VSMOW}$ except when dolomite data is sparse in the earliest Neoproterozoic ($\geq$805 Ma)(Fig. 3B). This aligns well with petrographic, crystallographic and spatial evidence that Neoproterozoic dolomite formed on or near the seafloor as proto-dolomite or dolomite in shallow marine environments, and stabilized as dolomite in the shallow sediments without significant fluid-alteration (*38–40*). This temperature similarity does not hold for locations in the Neoproterozoic with lower limestone δ^{18}O values indicative of more deeply buried strata (Fig. S6). In contrast, early Phanerozoic dolomite is clearly 'hotter' under Scenario 1, the constant seawater δ^{18}O assumption (Fig. 3B,Fig. S7). This distinction aligns well with petrographic evidence that early Phanerozoic dolomite is often fabric destruc-

tive and forms from fluid-buffered alteration at some point during burial (*20, 41*). Together these results indicate shallow marine Neoproterozoic environments were conducive to dolomite or proto-dolomite formation (i.e. high temperatures or high dissolved silica, etc.) (*38, 42*).

Temperature can be strongly coupled to the carbon cycle, through feedbacks with enhanced volcanic outgassing, organic matter remineralization, organic matter burial, terrestrial organic matter addition to marine environments, ocean CO_2 outgassing, or methane clathrate destabilization (i.e., (*43, 44*)). Both carbon cycle trends and alteration can impact the carbon isotopic composition of marine carbonates (i.e., (*43–46*)). We assess the δ^{13}C variability across materials and mineralogies through time keeping both alteration and carbon cycle processes in mind. In general, the limestone record is even more similar to the fossil record in δ^{13}C values than δ^{18}O values, in both distribution and variance, because carbon isotopes are more robust to alteration (Fig. 3D,E). While the δ^{13}C values of Neoproterozoic dolomite and limestone often diverge, we note the significant variability in the record itself during this time interval. Some large carbon isotope excursions have a temporal mineralogical signal across them (*47, 48*). Dolomite and limestone are often forming in shallow and deeper water environments in the Neoproterozoic, respectively (*40*). Their divergence may also reflect a water column depth gradient in δ^{13}C (*49*).

Constructing a long-term temperature record We filter the dataset by only including the 1^{st} to 50^{th} quantiles of Scenario 1 temperature to minimize outliers from meteoric or burial alteration. We use the 25^{th} to 75^{th} quantiles of δ^{13}C because alteration affects both extremes in this proxy. We opt to use limestone and shallow marine coastal fossil and planktonic foraminifera data from the entire available record (Fig. 3C,F, Fig. 4). We only use dolomite data from the Neoproterozoic younger than 805 Ma, because of dolomite sampling limitations in the earliest Neoproterozoic and exclude Phanerozoic dolomite data completely because of the mismatch in the Phanerzoic dolomite and limestone records (Fig. 3C,F). We explore the effects of excluding

dolomite, open ocean planktonic foraminfera, coastal fossils and planktonic foraminifera from the subtropics, all fossils, and all rocks. Despite the potential for a cool bias in the Cretaceous and Cenozoic from including open ocean planktonic foraminifera and Northern hemisphere subtropic fossils (*15, 18*), we find excluding these datasets only subtly alters the temperature record on the timescales we are considering and significantly reduces data density (Fig. S2). Excluding all dolomite from the record leads to cooler temperatures in the Ediacaran (Fig. S2,S3,S4). We opt for data density despite subtle temperature effects (Fig. S2). As a whole, this estimate is a warm-biased temperature record particularly in the early Phanerozoic and Precambrian because samples are dominated by tropical, coastal environments including higher temperature peritidal environments (*15, 18*).

The Scenario 1 temperature record from δ^{18}O suggests the Neoproterozoic experienced short-term fluctuations with hot coastal temperatures followed by long-term cooling including into Snowball Earth glaciations. This trend may be evidence for the 'Fire and Ice' model for Snowball Earth initiation (*50*)(Fig. 4). Carbonate rocks capturing the Sturtian Snowball Earth glaciation (660-717 Ma) (*51*) record some of the most enriched mineral δ^{18}O values in tropical environments over the last billion years, and thus the coldest extrapolated temperatures in Scenario 1 (Fig. 4) (*14*). The Ediacaran was cooler than the Tonian except for a few high temperature fluctuations. The first third of the Phanerozoic is characterized by high temperature fluctuations followed by significant cooling in both the middle Ordovician and early Carboniferous from coastal equatorial temperatures near 40°C to $\sim$20°C. Climate events co-occur with δ^{13}C perturbations across the entire record (*43*). In periods with known glacial deposits (blue bars in Fig. 1,3,4), we observe cooler temperatures than surrounding rocks in agreement with published Δ_{47} studies (*13, 14, 21*)(Fig. 4).

We identify four potential sources of error for earliest Phanerozoic and Neoproterozoic temperature in the current approach: [1] shallow, coastal Precambrian dolomite might form in more evaporatively ^{18}O-enriched water, which would make the record appear colder than it is (but see Fig. S2,S3,S4); [2] Neoproterozoic oceans may have been dominated by aragonite precipitation similar to the Late Paleozoic (*52*), and thus are perhaps more susceptible to δ^{18}O alteration as a population due to the metastability of aragonite, which could make the record appear hotter than it is; [3] limestone and dolomite δ^{18}O mineral values may have been more prone to alteration before shells were a part of the carbonate depositional environment, which would make the record appear hotter than it is; [4] sparse sampling could be biased by a few more altered locations negating a global sampling approach (i.e., the earliest Neoproterozoic, 1000–805 Ma). To account for these potential temperature offsets, more high-resolution paired δ^{18}O and Δ_{47}-temperature studies are necessary from well-preserved rocks in the Neoproterozoic.

Out of the twilight zone and into the tropics Life remained microscopic for at least three billion years of Earth's history. This persistent size restriction suggests that formidable evolutionary pressures kept life small. The consensus view that low dissolved oxygen concentrations was the dominant environmental parameter keeping Precambrian life microscopic and single-celled (*53*), has limitations (*54*). For example, marine oxygen concentrations were likely spatially variable following the Great Oxidation Event as evidenced by proxy variability (i.e., (*55*)). Furthermore, modern observations and experiments indicate that some macroscopic animals can grow in exceedingly low oxygen conditions (*56*). These details highlight that an overlooked alternative environmental control, such as temperature, may be critical to the tempo of evolutionary diversification.

Our temperature record in the Neoproterozoic and early Phanerozoic—the interval of time when complex, multicellular, macroscopic life evolved and thrived—is punctuated by higher-

frequency temperature fluctuations. We calculate per capita extinction and origination rates for the Cambrian and Ordovician using occurrence data from (*57*) and the rest of the Phanerozoic from (*58, 59*) and for the Neoproterozoic using occurrences of microscopic fossil populations (*60–62*) and macroscopic Ediacaran fauna (*63*)(Fig. 4). In the Phanerozoic, temperature increases are often associated with increased rates of extinction following by increased intensity of origination (*64*); this pattern is particularly evident in the early Cambrian (Fig. 4). In the Neoproterozoic, high temperature fluctuations co-occur with negative carbon isotope excursions like the mid-Ediacaran Shuram excursion and Bitter Springs excursions and extinction events for nascent complex life (*47*)(Fig. 4). Origination rates increase after these high temperature fluctuations (i.e. the late Ediacaran diversification of macroscopic soft bodied fauna).

Support for the controlling effect of temperature—both the long-term cooling trend and short-term fluctuations—on Earth's habitability through time comes from the fossil record in four forms: [1] a long-term cooling trend is supported by the microscopic body size of almost all taxa for much of the Neoproterozoic (see (*65*)). In the modern, high temperature environments limit the size of both larvae and adult ectotherms and endotherms; [2] both long-term cooling and short-term fluctuations in temperature are supported by the fact that macroscopic fauna appear first in deep water refugia, which likely experienced less temperature fluctuation and cooler overall temperatures (*54, 65, 66*). The first shallow water Ediacaran fossils appear after a 20-million year lag (Fig. 4); [3] both microscopic and macroscopic eukaryotic lagerstätte appear in the strata between high-temperature fluctuations in our record, which coincide with large negative carbon isotope excursions like the Bitter Springs and Shuram excursions (*23, 24, 47, 54, 60–62*)(Fig. 4); [4] extinction intensity (%) is elevated associated with high temperature fluctuations (i.e., the Shuram excursion, much of the Cambrian, the end-Devonian, and the end Permian) and origination intensity (%) is high in the cooler aftermaths (Fig. 4).

Long-term cooling trends may reflect coupling between tectonic drivers of climate change (i.e., (*67*)) and long-term changing reservoir sizes from enhanced carbon sequestration into carbonate sediments and organic matter deposition on flooded continental crust in the early Paleozoic (*68, 69*), into terrestrial biomass following land plant evolution (*70*), and into deep marine carbonates following the diversification of planktonic biomineralizing organisms in the Cretaceous and Cenozoic (*71, 72*)(Fig. 4). Our record suggests that by the second half of the Phanerozoic, equatorial sea surface temperatures remained below extinction thresholds for many macroscopic, complex animals even during climate perturbations, providing a mechanism for the observed decrease in extinction and origination intensities over the Phanerozoic (*73*). The Cambrian and early Ordovician peak in extinction and origination intensities was previously poorly linked to environmental oxygen change (*55*). We find evidence that short-term temperature fluctuations were an important environmental driver of evolutionary patterns during this time.

Conclusions Our record suggests the dogma about the fallibility of the oxygen isotopic composition of carbonate rocks can be overcome with statistical treatment of large, global, high-resolution compilations. Pairing clumped isotope thermometry and a data-rich oxygen isotope compilation reveals that shallow marine temperature change, not seawater oxygen isotope evolution, is the primary cause of the long term increase in the oxygen isotope composition of carbonate rocks over the last billion years. We find that well-documented Cenozoic cooling (*5*) pales in comparison to the long-term cooling in tropical, shallow marine environments in Earth's more distant past. On shorter timescales, the record captures cooling and warming associated with known glacial-greenhouse transitions in both the Proterozoic and Phanerozoic. These short-term temperature fluctuations decrease in magnitude through time which is mirrored in reduced extinction and origination intensities and smaller δ^{13}C excursions. We find evidence

that high temperature episodes were bottlenecks for complex life and cooling following higher temperature fluctuations allowed for origination and diversification.

Acknowledgements K.D.B. is grateful to Andy Knoll for providing a sample suite analyzed in this study from multiple Neoproterozoic field sites. K.D.B. thanks Clint Cowan for providing comments on early drafts of this work and for being a sounding board for ideas.

Funding K.D.B. acknowledges funding from the Packard Foundation and NASA Exobiology Grant 80NSSC19K0464. M.D.C. was supported by a National Defense Science and Engineering Graduate Fellowship. Research was conducted and permitted under the Research in Svalbard (RIS) ID 6867.

Author Contributions K.D.B. conceptualized the study, developed the methodology, and wrote the original draft. N.B. and K.D.B contributed software, formal analysis and visualization. K.D.B, J.W.C., J.D., and O.L. contributed data curation. K.D.B, J.W., and N.T.A. supervised data curation. All authors reviewed and edited the manuscript.

Data and materials availability All data are provided in the supplementary materials. Upon manuscript acceptance, unpublished data, figures and code will be made available on Open Science Framework (link).

Supplementary Materials :

Materials and Methods

Figs. S1 - S7

References (74 - 221)

References and Notes

1. J. Veizer, P. Bruckschen, F. Pawellek, A. Diener, O. G. Podlaha, G. A. F. Carden, T. Jasper, C. Korte, H. Strauss, K. Azmy, D. Ala, Oxygen isotope evolution of Phanerozoic seawater. *Palaeogeogr. Palaeoclimatol. Palaeoecol.* **132**, 159–172 (1997).

2. J. B. D. Jaffrés, G. A. Shields, K. Wallmann, The oxygen isotope evolution of seawater: A critical review of a long-standing controversy and an improved geological water cycle model for the past 3.4 billion years. *Earth-Science Rev.* **83**, 83–122 (2007).

3. N. Galili, A. Shemesh, R. Yam, I. Brailovsky, M. Sela-Adler, E. M. Schuster, C. Collom, A. Bekker, N. Planavsky, F. A. Macdonald, A. Préat, M. Rudmin, W. Trela, U. Sturesson, J. M. Heikoop, M. Aurell, J. Ramajo, I. Halevy, The geologic history of seawater oxygen isotopes from marine iron oxides. *Science* **365**, 469–473 (2019).

4. J. C. G. Walker, P. B. Hays, J. F. Kasting, A negative feedback mechanism for the long-term stabilization of Earth's surface temperature. *J. Geophys. Res. Ocean.* **86**, 9776–9782 (1981).

5. T. Westerhold, N. Marwan, A. J. Drury, D. Liebrand, C. Agnini, E. Anagnostou, J. S. K. Barnet, S. M. Bohaty, D. De Vleeschouwer, F. Florindo, T. Frederichs, D. A. Hodell, A. E. Holbourn, D. Kroon, V. Lauretano, K. Littler, L. J. Lourens, M. Lyle, H. Pälike, U. Röhl, J. Tian, R. H. Wilkens, P. A. Wilson, J. C. Zachos, An astronomically dated record of Earth's climate and its predictability over the last 66 million years. *Science* **369**, 1383–1387 (2020).

6. E. L. Grossman, M. M. Joachimski, Ocean temperatures through the Phanerozoic re-assessed. *Scientific Reports* **12**, 1–13 (2022).

7. J. A. Trotter, I. S. Williams, C. R. Barnes, C. Lécuyer, R. S. Nicoll, Did cooling oceans trigger Ordovician biodiversification? Evidence from conodont thermometry. *Science* **321**, 550–554 (2008).

8. L. P. Knauth, D. R. Lowe, High Archean climatic temperature inferred from oxygen isotope geochemistry of cherts in the 3.5 Ga Swaziland Supergroup, South Africa. *Bull. Geol. Soc. Am.* **115**, 566–580 (2003).

9. F. Robert, M. Chaussidon, A palaeotemperature curve for the Precambrian oceans based on silicon isotopes in cherts. *Nature* **443**, 969–972 (2006).

10. F. L. Liljestrand, A. H. Knoll, N. J. Tosca, P. A. Cohen, F. A. Macdonald, Y. Peng, D. T. Johnston, The triple oxygen isotope composition of Precambrian chert. *Earth and Planetary Science Letters* **537**, 116167 (2020).

11. J. M. Eiler, "Clumped-isotope" geochemistry-The study of naturally-occurring, multiply-substituted isotopologues. *Earth Planet. Sci. Lett.* **262**, 309–327 (2007).

12. K. D. Bergmann, S. Finnegan, R. Creel, J. M. Eiler, N. C. Hughes, L. E. Popov, W. W. Fischer, A paired apatite and calcite clumped isotope thermometry approach to estimating Cambro-Ordovician seawater temperatures and isotopic composition. *Geochim. Cosmochim. Acta* **224**, 18–41 (2018).

13. K. D. Bergmann, S. A. Al Balushi, T. J. MacKey, J. P. Grotzinger, J. M. Eiler, A 600-million-year carbonate clumped-isotope record from the Sultanate of Oman. *J. Sediment. Res.* **88**, 960–979 (2018).

14. T. J. Mackey, A. B. Jost, J. R. Creveling, K. D. Bergmann, A decrease to low carbonate clumped isotope temperatures in Cryogenian strata. *AGU Adv.* **1** (2020).

15. E. J. Judd, T. Bhattacharya, L. C. Ivany, A Dynamical Framework for Interpreting Ancient Sea Surface Temperatures. *Geophys. Res. Lett.* **47** (2020).

16. E. Grossman, M. Joachimski, Oxygen isotope stratigraphy. *Geologic Time Scale 2020* (Elsevier, 2020), pp. 279–307.

17. J. B. Ries, Review: geological and experimental evidence for secular variation in seawater Mg/Ca (calcite-aragonite seas) and its effects on marine biological calcification. *Biogeosciences* **7**, 2795–2849 (2010).

18. L. A. Jones, K. Eichenseer, Uneven spatial sampling distorts reconstructions of Phanerozoic seawater temperature. *Geology* **50**, 238–242 (2022).

19. G. A. Henkes, B. H. Passey, E. L. Grossman, B. J. Shenton, T. E. Yancey, A. Pérez-Huerta, Temperature evolution and the oxygen isotope composition of Phanerozoic oceans from carbonate clumped isotope thermometry. *Earth Planet. Sci. Lett.* **490**, 40–50 (2018).

20. U. Ryb, J. M. Eiler, Oxygen isotope composition of the Phanerozoic ocean and a possible solution to the dolomite problem. *Proc. Natl. Acad. Sci. U. S. A.* **115**, 6602–6607 (2018).

21. S. Finnegan, K. Bergmann, J. Eiler, D. Jones, D. Fike, I. Eisenman, N. Hughes, A. Tripati, W. Fischer, The magnitude and duration of late Ordovician-early Silurian glaciation. *Science* **331** (2011).

22. F. M. Gradstein, J. G. Ogg, M. D. Schmitz, G. M. Ogg, *Geologic time scale 2020* (Elsevier, 2020).

23. A. D. Rooney, M. D. Cantine, K. D. Bergmann, I. Gómez-Pérez, B. A. Baloushi, T. H. Boag, J. F. Busch, E. A. Sperling, J. V. Strauss, Calibrating the coevolution of Ediacaran life and environment. *Proc. Natl. Acad. Sci. U. S. A.* **117**, 16824–16830 (2020).

24. C. Yang, A. D. Rooney, D. J. Condon, X.-H. Li, D. V. Grazhdankin, F. T. Bowyer, C. Hu, F. A. Macdonald, M. Zhu, The tempo of Ediacaran evolution. *Science Advances* **7**, eabi9643 (2021).

25. Y. Park, N. L. Swanson-Hysell, S. A. MacLennan, A. C. Maloof, M. Gebreslassie, M. M. Tremblay, B. Schoene, M. Alene, E. S. Anttila, T. Tesema, B. Haileab, The lead-up to the Sturtian Snowball Earth: Neoproterozoic chemostratigraphy time-calibrated by the Tambien Group of Ethiopia. *GSA Bull.* **132**, 1119–1149 (2020).

26. S. T. Kim, J. R. O'Neil, Equilibrium and nonequilibrium oxygen isotope effects in synthetic carbonates. *Geochim. Cosmochim. Acta* **61**, 3461–3475 (1997).

27. J. Horita, Oxygen and carbon isotope fractionation in the system dolomite–water–CO_2 to elevated temperatures. *Geochim. Cosmochim. Acta* **129**, 111–124 (2014).

28. C. H. Lear, Cenozoic Deep-Sea Temperatures and Global Ice Volumes from Mg/Ca in Benthic Foraminiferal Calcite. *Science* **287**, 269–272 (2000).

29. B. S. Cramer, K. G. Miller, P. J. Barrett, J. D. Wright, Late Cretaceous-Neogene trends in deep ocean temperature and continental ice volume: Reconciling records of benthic foraminiferal geochemistry (δ^{18}O and Mg/Ca) with sea level history. *J. Geophys. Res. Ocean.* **116**, C12023 (2011).

30. Materials and methods are available as supplementary materials at the science website .

31. F. Hodel, M. Macouin, R. I. F. Trindade, A. Triantafyllou, J. Ganne, V. Chavagnac, J. Berger, M. Rospabé, C. Destrigneville, J. Carlut, N. Ennih, P. Agrinier, Fossil black smoker yields oxygen isotopic composition of Neoproterozoic seawater. *Nat. Commun.* **9**, 1453 (2018).

32. K. Muehlenbachs, R. N. Clayton, Oxygen isotope composition of the oceanic crust and its bearing on seawater. *J. Geophys. Res.* **81**, 4365–4369 (1976).

33. C. Holmden, K. Muehlenbachs, The $^{18}O/^{16}O$ Ratio of 2-Billion-Year-Old Seawater Inferred from Ancient Oceanic Crust. *Science* **259**, 1733–6 (1993).

34. P. Gilbert, K. Bergmann, C. Myers, M. Marcus, R. DeVol, C.-Y. Sun, A. Blonsky, E. Tamre, J. Zhao, E. Karan, N. Tamura, S. Lemer, A. Giuffre, G. Giribet, J. Eiler, A. Knoll, Nacre tablet thickness records formation temperature in modern and fossil shells. *Earth Planet. Sci. Lett.* **460** (2017).

35. S. L. Goldberg, T. M. Present, S. Finnegan, K. D. Bergmann, A high−resolution record of early Paleozoic climate. *Proceedings of the National Academy of Sciences* **118** (2021).

36. J. B. Ries, Review: geological and experimental evidence for secular variation in seawater Mg/Ca (calcite-aragonite seas) and its effects on marine biological calcification. *Biogeosciences* **7**, 2795–2849 (2010).

37. P. K. Swart, 8. THE OXYGEN ISOTOPIC COMPOSITION OF INTERSTITIAL WATERS: EVIDENCE FOR FLUID FLOW AND RECRYSTALLIZATION IN THE MARGIN OF THE GREAT BAHAMA BANK 1 (2000).

38. J. Wilcots, P. Gilbert, K. Bergmann, Nanoscale crystal fabric preserved in dolomite ooids at the onset of the Ediacaran Shuram excursion. *Geophysical Research Letters* (PrePrint).

39. M. E. Tucker, Precambrian dolomites: petrographic and isotopic evidence that they differ from Phanerozoic dolomites. *Geology* **10**, 7–12 (1982).

40. M. D. Cantine, A. H. Knoll, K. D. Bergmann, Carbonates before skeletons: A database approach. *Earth-Science Reviews* **201**, 103065 (2020).

41. F. A. Corsetti, D. L. Kidder, P. J. Marenco, Trends in oolite dolomitization across the Neoproterozoic-Cambrian boundary: A case study from Death Valley, California. *Sediment. Geol.* **191**, 135–150 (2006).

42. Y. Fang, H. Xu, Dissolved silica-catalyzed disordered dolomite precipitation. *American Mineralogist: Journal of Earth and Planetary Materials* **107**, 443–452 (2022).

43. S. M. Stanley, Relation of Phanerozoic stable isotope excursions to climate, bacterial metabolism, and major extinctions. *Proc. Natl. Acad. Sci. U. S. A.* **107**, 19185–19189 (2010).

44. S. K. Turner, Pliocene switch in orbital-scale carbon cycle/climate dynamics. *Paleoceanography* **29**, 1256–1266 (2014).

45. P. K. Swart, M. J. Kennedy, Does the global stratigraphic reproducibility of δ13C in Neoproterozoic carbonates require a marine origin? A Pliocene–Pleistocene comparison. *Geology* (2012).

46. L. A. Derry, A burial diagenesis origin for the Ediacaran Shuram-Wonoka carbon isotope anomaly. *Earth Planet. Sci. Lett.* **294**, 152–162 (2010).

47. K. D. Bergmann, M. R. Osburn, J. Wilcots, M. D. Cantine, J. P. Grotzinger, W. W. Fischer, J. M. Eiler, M. Bonifacie, The Shuram excursion: A response to climate extremes at the dawn of animal life. *Preprint at 10.1002/essoar.10511917.1* (2022).

48. J. F. Busch, E. B. Hodgin, A.-S. C. Ahm, J. M. Husson, F. A. Macdonald, K. D. Bergmann, J. A. Higgins, J. V. Strauss, Global and local drivers of the Ediacaran Shuram carbon isotope excursion. *Earth and Planetary Science Letters* **579**, 117368 (2022).

49. G. Jiang, A. J. Kaufman, N. Christie-Blick, S. Zhang, H. Wu, Carbon isotope variability across the Ediacaran Yangtze platform in South China: Implications for a large surface-to-deep ocean δ^{13}C gradient. *Earth Planet. Sci. Lett.* **261**, 303–320 (2007).

50. Y. Goddéris, Y. Donnadieu, A. Nédélec, B. Dupré, C. Dessert, A. Grard, G. Ramstein, L. M. François, The Sturtian 'snowball' glaciation: Fire and ice. *Earth Planet. Sci. Lett.* **211**, 1–12 (2003).

51. A. D. Rooney, J. V. Strauss, A. D. Brandon, F. A. Macdonald, A Cryogenian chronology: Two long-lasting synchronous neoproterozoic glaciations. *Geology* **43**, 459–462 (2015).

52. A. van Smeerdijk Hood, M. W. Wallace, Neoproterozoic marine carbonates and their paleoceanographic significance. *Global and Planetary Change* **160**, 28–45 (2018).

53. T. W. Lyons, C. T. Reinhard, N. J. Planavsky, The rise of oxygen in Earth's early ocean and atmosphere. *Nature* **506**, 307–15 (2014).

54. F. Zhang, H. Wang, Y. Ye, Y. Liu, Y. Lyu, Y. Deng, D. Lyu, X. Wang, H. Wu, S. Deng, *et al.*, Did high temperature rather than low O_2 hinder the evolution of eukaryotes in the Precambrian? *Precambrian Research* **378**, 106755 (2022).

55. E. A. Sperling, C. A. Frieder, A. V. Raman, P. R. Girguis, L. A. Levin, A. H. Knoll, Oxygen, ecology, and the Cambrian radiation of animals. *Proc. Natl. Acad. Sci. U. S. A.* **110**, 13446–51 (2013).

56. D. B. Mills, L. M. Ward, C. Jones, B. Sweeten, M. Forth, A. H. Treusch, D. E. Canfield, Oxygen requirements of the earliest animals. *Proceedings of the National Academy of Sciences* **111**, 4168–4172 (2014).

57. C. M. Rasmussen, B. Kröger, M. L. Nielsen, J. Colmenar, Cascading trend of Early Paleozoic marine radiations paused by Late Ordovician extinctions. *Proceedings of the National Academy of Sciences* **116**, 7207–7213 (2019).

58. Ádám T. Kocsis, divDyn/ddPhanero: Phanerozoic-level diversity analyses with the R package divDyn (2019).

59. (the r package divdyn for quantifying diversity dynamics using fossil sampling data .

60. K. A. McFadden, J. Huang, X. Chu, G. Jiang, A. J. Kaufman, C. Zhou, X. Yuan, S. Xiao, Pulsed oxidation and biological evolution in the Ediacaran Doushantuo Formation. *Proc. Natl. Acad. Sci.* **105**, 3197–3202 (2008).

61. L. A. Riedman, P. M. Sadler, Global species richness record and biostratigraphic potential of early to middle Neoproterozoic eukaryote fossils. *Precambrian Res.* **319**, 6–18 (2018).

62. S. Xiao, B. Shen, Q. Tang, A. J. Kaufman, X. Yuan, J. Li, M. Qian, Biostratigraphic and chemostratigraphic constraints on the age of early Neoproterozoic carbonate successions in North China. *Precambrian Res.* **246**, 208–225 (2014).

63. T. H. Boag, S. A. Darroch, M. Laflamme, Ediacaran distributions in space and time: Testing assemblage concepts of earliest macroscopic body fossils. *Paleobiology* **42**, 574–594 (2016).

64. H. Song, D. B. Kemp, L. Tian, D. Chu, H. Song, X. Dai, Thresholds of temperature change for mass extinctions. *Nature communications* **12**, 1–8 (2021).

65. C. Simpson, Adaptation to a viscous Snowball Earth ocean as a path to complex multicellularity. *The American Naturalist* **198**, 590–609 (2021).

66. T. H. Boag, R. G. Stockey, L. E. Elder, P. M. Hull, E. A. Sperling, Oxygen, temperature and the deep-marine stenothermal cradle of Ediacaran evolution. *Proc. R. Soc. B Biol. Sci.* **285**, 20181724 (2018).

67. F. A. Macdonald, N. L. Swanson-Hysell, Y. Park, L. Lisiecki, O. Jagoutz, Arc-continent collisions in the tropics set Earth's climate state. *Science* **364**, 181–184 (2019).

68. K. D. Bergmann, J. Wilcots, T. Pico, N. Boekelheide, N. T. Anderson, M. D. Cantine, S. L. Goldberg, B. Keller, A. B. Jost, A. Eyster, Onset of carbonate biomineralization drove global reorganization of sedimentation and subsidence patterns. *Preprint at 10.1002/essoar.10511913.1* (2022).

69. J. M. Husson, S. E. Peters, Atmospheric oxygenation driven by unsteady growth of the continental sedimentary reservoir. *Earth Planet. Sci. Lett.* **460**, 68–75 (2017).

70. T. W. Dahl, S. K. Arens, The impacts of land plant evolution on Earth's climate and oxygenation state–An interdisciplinary review. *Chemical Geology* **547**, 119665 (2020).

71. A. Ridgwell, R. E. Zeebe, The role of the global carbonate cycle in the regulation and evolution of the Earth system. *Earth Planet. Sci. Lett.* **234**, 299–315 (2005).

72. J. M. Edmond, Y. Huh, Non-steady state carbonate recycling and implications for the evolution of atmospheric pCO_2. *Earth Planet. Sci. Lett.* **216**, 125–139 (2003).

73. J. Alroy, M. Aberhan, D. J. Bottjer, M. Foote, F. T. Fürsich, P. J. Harries, A. J. Hendy, S. M. Holland, L. C. Ivany, W. Kiessling, M. A. Kosnik, C. R. Marshall, A. J. McGowan, A. I. Miller, T. D. Olszewski, M. E. Patzkowsky, S. E. Peters, L. Villier, P. J. Wagner, N. Bonuso, P. S. Borkow, B. Brenneis, M. E. Clapham, L. M. Fall, C. A. Ferguson, V. L. Hanson, A. Z. Krug, K. M. Layou, E. H. Leckey, S. Nürnberg, C. M. Powers, J. A. Sessa,

C. Simpson, A. Tomašových, C. C. Visaggi, Phanerozoic trends in the global diversity of marine invertebrates. *Science* **321**, 97–100 (2008).

74. M. Foote, Origination and extinction components of taxonomic diversity: general problems. *Paleobiology* **26**, 74–102 (2000).

75. K. D. T. Nguyen, S. A. Morley, C. H. Lai, M. S. Clark, K. S. Tan, A. E. Bates, L. S. Peck, Upper temperature limits of tropical marine ectotherms: Global warming implications. *PLoS One* **6** (2011).

76. A. H. Knoll, A. J. Kaufman, M. A. Semikhatov, The carbon-isotopic composition of Proterozoic carbonates: Riphean successions from northwestern Siberia (Anabar Massif, Turukhansk uplift). *Am. J. Sci.* **295**, 823–850 (1995).

77. A. H. Knoll, R. K. Bambach, D. E. Canfield, J. P. Grotzinger, Comparative Earth history and Late Permian mass extinction. *Science* **273**, 452–457 (1996).

78. L. C. Kah, A. G. Sherman, G. M. Narbonne, A. H. Knoll, A. J. Kaufman, δ^{13}C stratigraphy of the Proterozoic Bylot Supergroup, Baffin Island, Canada: implications for regional lithostratigraphic correlations. *Can. J. Earth Sci.* **36**, 313–332 (1999).

79. G. J. Gilleaudeau, L. C. Kah, Carbon isotope records in a Mesoproterozoic epicratonic sea: Carbon cycling in a low-oxygen world. *Precambrian Res.* **228**, 85–101 (2013).

80. L. C. Kah, J. K. Bartley, D. A. Teal, Chemostratigraphy of the Late Mesoproterozoic Atar Group, Taoudeni Basin, Mauritania: Muted isotopic variability, facies correlation, and global isotopic trends. *Precambrian Res.* **200-203**, 82–103 (2012).

81. H. Guo, Y. Du, L. C. Kah, J. Huang, C. Hu, H. Huang, W. Yu, Isotopic composition of organic and inorganic carbon from the Mesoproterozoic Jixian Group, North China: Implications for biological and oceanic evolution. *Precambrian Res.* **224**, 169–183 (2013).

82. Y. Sawaki, T. Ohno, M. Tahata, T. Komiya, T. Hirata, S. Maruyama, B. F. Windley, J. Han, D. Shu, Y. Li, The Ediacaran radiogenic Sr isotope excursion in the Doushantuo Formation in the Three Gorges area, South China. *Precambrian Res.* **176**, 46–64 (2010).

83. D. A. Fike, J. P. Grotzinger, L. M. Pratt, R. E. Summons, Oxidation of the Ediacaran ocean. *Nature* **444**, 744–747 (2006).

84. M. R. Osburn, J. Owens, K. D. Bergmann, T. W. Lyons, Dynamic changes in sulfate sulfur isotopes preceding the Ediacaran Shuram Excursion. *Geochim. Cosmochim. Acta* (2015).

85. G. Jiang, X. Wang, X. Shi, S. Xiao, S. Zhang, J. Dong, The origin of decoupled carbonate and organic carbon isotope signatures in the early Cambrian (ca. 542-520Ma) Yangtze platform. *Earth Planet. Sci. Lett.* **317-318**, 96–110 (2012).

86. C. Lee, G. D. Love, W. W. Fischer, J. P. Grotzinger, G. P. Halverson, Marine organic matter cycling during the Ediacaran Shuram excursion. *Geology* **43**, 1103–1106 (2015).

87. C. Li, D. S. Hardisty, G. Luo, J. Huang, T. J. Algeo, M. Cheng, W. Shi, Z. An, J. Tong, S. Xie, N. Jiao, T. W. Lyons, Uncovering the spatial heterogeneity of Ediacaran carbon cycling. *Geobiology* **15**, 211–224 (2017).

88. B. G. Pokrovskii, V. A. Melezhik, M. I. Bujakaite, Carbon, oxygen, strontium, and sulfur isotopic compositions in late Precambrian rocks of the Patom Complex, central Siberia: Communication 1. results, isotope stratigraphy, and dating problems. *Lithol. Miner. Resour.* **41**, 450–474 (2006).

89. M. Tahata, Y. Ueno, T. Ishikawa, Y. Sawaki, K. Murakami, J. Han, D. Shu, Y. Li, J. Guo, N. Yoshida, T. Komiya, Carbon and oxygen isotope chemostratigraphies of the Yangtze platform, South China: Decoding temperature and environmental changes through the Ediacaran. *Gondwana Res.* **23**, 333–353 (2013).

90. X. Wang, G. Jiang, X. Shi, S. Xiao, Paired carbonate and organic carbon isotope variations of the Ediacaran Doushantuo Formation from an upper slope section at Siduping, South China. *Precambrian Res.* **273**, 53–66 (2016).

91. T. Ishikawa, Y. Ueno, T. Komiya, Y. Sawaki, J. Han, D. Shu, Y. Li, S. Maruyama, N. Yoshida, Carbon isotope chemostratigraphy of a Precambrian/Cambrian boundary section in the Three Gorge area, South China: Prominent global-scale isotope excursions just before the Cambrian Explosion. *Gondwana Res.* **14**, 193–208 (2008).

92. R. Kikumoto, M. Tahata, M. Nishizawa, Y. Sawaki, S. Maruyama, D. Shu, J. Han, T. Komiya, K. Takai, Y. Ueno, Nitrogen isotope chemostratigraphy of the Ediacaran and Early Cambrian platform sequence at Three Gorges, South China. *Gondwana Res.* **25**, 1057–1069 (2014).

93. G. M. Cox, G. P. Halverson, A. Poirier, D. Le Heron, J. V. Strauss, R. Stevenson, A model for Cryogenian iron formation. *Earth Planet. Sci. Lett.* **433**, 280–292 (2016).

94. G. P. Halverson, A. C. Maloof, P. F. Hoffman, The Marinoan glaciation (Neoproterozoic) in northeast Svalbard. *Basin Res.* **16**, 297–324 (2004).

95. G. P. Halverson, P. F. Hoffman, D. P. Schrag, A. J. Kaufman, A major perturbation of the carbon cycle before the Ghaub glaciation (Neoproterozoic) in Namibia: Prelude to snowball Earth? *Geochemistry, Geophys. Geosystems* **3**, 1–24 (2002).

96. G. P. Halverson, P. F. Hoffman, D. P. Schrag, A. C. Maloof, A. H. N. Rice, Toward a Neoproterozoic composite carbon-isotope record. *Bull. Geol. Soc. Am.* **117**, 1181–1207 (2005).

97. G. P. Halverson, A. C. Maloof, D. P. Schrag, F. Ö. Dudás, M. Hurtgen, Stratigraphy and geochemistry of a ca 800 Ma negative carbon isotope interval in northeastern Svalbard. *Chem. Geol.* **237**, 23–45 (2007).

98. D. T. Johnston, F. A. Macdonald, B. C. Gill, P. F. Hoffman, D. P. Schrag, Uncovering the Neoproterozoic carbon cycle. *Nature* **483** (2012).

99. A. B. Kuznetsov, M. A. Semikhatov, A. V. Maslov, I. M. Gorokhov, E. M. Prasolov, M. T. Krupenin, I. V. Kislova, New data on Sr-and C-isotopic chemostratigraphy of the Upper Riphean type section (southern Urals). *Stratigr. Geol. Correl.* **14**, 602–628 (2006).

100. N. L. Swanson-Hysell, C. V. Rose, C. C. Calmet, G. P. Halverson, M. T. Hurtgen, A. C. Maloof, Cryogenian glaciation and the onset of carbon-isotope decoupling. *Science* **328**, 608–611 (2010).

101. H. Bao, I. J. Fairchild, P. M. Wynn, C. Spötl, Stretching the envelope of past surface environments: Neoproterozoic glacial lakes from Svalbard. *Science* **323**, 119–122 (2009).

102. A.-S. C. Ahm, C. J. Bjerrum, P. F. Hoffman, F. A. Macdonald, A. C. Maloof, C. V. Rose, J. V. Strauss, J. A. Higgins, The Ca and Mg isotope record of the Cryogenian Trezona carbon isotope excursion. *Earth and Planetary Science Letters* **568**, 117002 (2021).

103. P. C. Boggiani, C. Gaucher, A. N. Sial, M. Babinski, C. M. Simon, C. Riccomini, V. P. Ferreira, T. R. Fairchild, Chemostratigraphy of the Tamengo Formation (Corumbá Group, Brazil): A contribution to the calibration of the Ediacaran carbon-isotope curve. *Precambrian Res.* **182**, 382–401 (2010).

104. F. J. Gomez, N. Ogle, R. A. Astini, R. M. Kalin, Paleoenvironmental and carbon-oxygen isotope record of Middle Cambrian carbonates (La Laja Formation) in the Argentine Precordillera. *J. Sediment. Res.* **77**, 826–842 (2007).

105. R. A. Howley, G. Jiang, The Cambrian Drumian carbon isotope excursion (DICE) in the Great Basin, western United States. *Palaeogeogr. Palaeoclimatol. Palaeoecol.* **296**, 138–150 (2010).

106. A. C. Maloof, S. M. Porter, J. L. Moore, F. Ö. Dudás, S. A. Bowring, J. A. Higgins, D. A. Fike, M. P. Eddy, The earliest Cambrian record of animals and ocean geochemical change. *Bull. Geol. Soc. Am.* **122**, 1731–1774 (2010).

107. A. N. Sial, S. Peralta, V. P. Ferreira, A. J. Toselli, F. G. Aceñolaza, M. A. Parada, C. Gaucher, R. N. Alonso, M. M. Pimentel, Upper Cambrian carbonate sequences of the Argentine Precordillera and the Steptoean C-Isotope positive excursion (SPICE). *Gondwana Res.* **13**, 437–452 (2008).

108. E. F. Smith, F. A. Macdonald, T. A. Petach, U. Bold, D. P. Schrag, Integrated stratigraphic, geochemical, and paleontological late Ediacaran to early Cambrian records from southwestern Mongolia. *Bull. Geol. Soc. Am.* **128**, 442–468 (2016).

109. C. K. Thompson, L. C. Kah, Sulfur isotope evidence for widespread euxinia and a fluctuating oxycline in Early to Middle Ordovician greenhouse oceans. *Palaeogeogr. Palaeoclimatol. Palaeoecol.* **313-314**, 189–214 (2012).

110. S. J. Loyd, P. J. Marenco, J. W. Hagadorn, T. W. Lyons, A. J. Kaufman, F. Sour-Tovar, F. A. Corsetti, Sustained low marine sulfate concentrations from the Neoproterozoic to the Cambrian: Insights from carbonates of northwestern Mexico and eastern California. *Earth Planet. Sci. Lett.* **339-340**, 79–94 (2012).

111. L. A. Derry, M. D. Brasier, R. M. Corfield, A. Y. Rozanov, A. Y. Zhuravlev, Sr and C isotopes in Lower Cambrian carbonates from the Siberian craton: A paleoenvironmental record during the 'Cambrian explosion'. *Earth Planet. Sci. Lett.* **128**, 671–681 (1994).

112. C. Chang, W. Hu, X. Wang, H. Yu, A. Yang, J. Cao, S. Yao, Carbon isotope stratigraphy of the lower to middle Cambrian on the eastern Yangtze Platform, South China. *Palaeogeography, Palaeoclimatology, Palaeoecology* **479**, 90–101 (2017).

113. L. Ainsaar, D. Kaljo, T. Martma, T. Meidla, P. Männik, J. Nõlvak, O. Tinn, Middle and Upper Ordovician carbon isotope chemostratigraphy in Baltoscandia: A correlation standard and clues to environmental history. *Palaeogeogr. Palaeoclimatol. Palaeoecol.* **294**, 189–201 (2010).

114. K. Azmy, I. Knight, D. Lavoie, G. Chi, Origin of dolomites in the Boat Harbour Formation, St. George Group, in western Newfoundland, Canada: Implications for porosity development. *Bull. Can. Pet. Geol.* **57**, 81–104 (2009).

115. K. Lynn Batten Hender, Mixed Siliciclastic-Carbonate ramp sediments and coral bioherms of the Late Ordovician Lourdes Formation, Western Newfoundland: Sedimentology, Stratigraphy, and Tectonic Significance, Ph.D. thesis, Carleton University (2007).

116. P. A. Brandl, Carbon and oxygen isotopes, stratigraphy, and facies of the Oslobreen Group (northeast Ny Friesland, Svalbard), Ph.D. thesis (2009).

117. C. T. Edwards, M. Saltzman, Paired carbon isotopic analysis of Ordovician bulk carbonate ($\delta^{13}C_{carb}$) and organic matter ($\delta^{13}C_{org}$) spanning the Great Ordovician Biodiversification Event. *Palaeogeogr. Palaeoclimatol. Palaeoecol.* **458**, 102–117 (2016).

118. A. Husinec, S. M. Bergström, Stable carbon-isotope record of shallow-marine evaporative epicratonic basin carbonates, Ordovician Williston Basin, North America. *Sedimentology* **62**, 314–349 (2015).

119. D. Kaljo, L. Hints, T. Martma, J. Nõlvak, A. Oraspõld, Late Ordovician carbon isotope trend in Estonia, its significance in stratigraphy and environmental analysis. *Palaeogeogr. Palaeoclimatol. Palaeoecol.* **210**, 165–185 (2004).

120. A. Lindskog, A. M. L. Lindskog, J. V. Johansson, P. Ahlberg, M. E. Eriksson, H. Smithsgatan, The Cambrian-Ordovician succession at Lanna, Sweden: stratigraphy and depositional environments. *Est. J. Earth Sci.* **67**, 133–148 (2018).

121. A. Mauviel, A. Desrochers, A high-resolution, continuous δ^{13}C record spanning the ordovician-silurian boundary on Anticosti Island, Eastern Canada. *Can. J. Earth Sci.* **53**, 795–801 (2016).

122. P. McLaughlin, P. Emsbo, A. Desrochers, A. Bancroft, C. Brett, J. Riva, W. Premo, L. Neymark, A. Achab, E. Asselin, M. Emmons, Refining 2 km of Ordovician chronostratigraphy beneath Anticosti Island utilizing integrated chemostratigraphy. *Can. J. Earth Sci.* **53**, 1–10 (2016).

123. P. C. Quinton, A. D. Herrmann, S. A. Leslie, K. G. MacLeod, Carbon cycling across the southern margin of Laurentia during the Late Ordovician. *Palaeogeogr. Palaeoclimatol. Palaeoecol.* **458**, 63–76 (2016).

124. C. M. Ø. Rasmussen, C. V. Ullmann, K. G. Jakobsen, A. Lindskog, J. Hansen, T. Hansen, M. E. Eriksson, A. Dronov, R. Frei, C. Korte, A. T. Nielsen, D. A. Harper, Onset of main Phanerozoic marine radiation sparked by emerging Mid Ordovician icehouse. *Sci. Rep.* **6**, 18884 (2016).

125. M. R. Saltzman, S. A. Young, L. R. Kump, B. C. Gill, T. W. Lyons, B. Runnegar, Pulse of atmospheric oxygen during the late Cambrian. *Proc. Natl. Acad. Sci. U. S. A.* **108**, 3876–3881 (2011).

126. S. Scorrer, K. Azmy, S. Stouge, Carbon-isotope stratigraphy of the Furongian Berry Head Formation (Port au Port Group) and Tremadocian Watts Bight Formation (St. George Group), western Newfoundland, and the correlative significance1. *Can. J. Earth Sci.* **56**, 223–234 (2019).

127. A. N. Sial, S. Peralta, C. Gaucher, A. J. Toselli, V. P. Ferreira, R. Frei, M. A. Parada, M. M. Pimentel, N. Silva Pereira, High-resolution stable isotope stratigraphy of the upper Cambrian and Ordovician in the Argentine Precordillera: Carbon isotope excursions and correlations. *Gondwana Res.* **24**, 330–348 (2013).

128. R. C. Wu, M. Calner, O. Lehnert, O. Peterffy, M. M. Joachimski, Lower-Middle Ordovician δ^{13}C chemostratigraphy of western Baltica (Jämtland, Sweden). *Palaeoworld* **24**, 110–122 (2015).

129. R. Wu, M. Calner, O. Lehnert, Integrated conodont biostratigraphy and carbon isotope chemostratigraphy in the Lower-Middle Ordovician of southern Sweden reveals a complete record of the MDICE. *Geol. Mag.* **154**, 334–353 (2017).

130. S. A. Young, M. R. Saltzman, S. M. Bergström, Upper Ordovician (Mohawkian) carbon isotope (δ^{13}C) stratigraphy in eastern and central North America: Regional expression of a perturbation of the global carbon cycle. *Palaeogeogr. Palaeoclimatol. Palaeoecol.* **222**, 53–76 (2005).

131. L. Zhang, T. J. Algeo, L. Cao, L. Zhao, Z. Q. Chen, Z. Li, Diagenetic uptake of rare earth elements by conodont apatite. *Palaeogeogr. Palaeoclimatol. Palaeoecol.* **458**, 176–197 (2016).

132. M. R. Saltzman, Silurian δ^{13}C stratigraphy: a view from North America. *Geology* **29**, 671–674 (2001).

133. N. E. McAdams, M. D. Schmitz, M. A. Kleffner, J. Verniers, T. R. Vandenbroucke, J. R. Ebert, B. D. Cramer, A new, high-precision CA-ID-TIMS date for the 'Kalkberg' K-bentonite (Judds Falls Bentonite). *Lethaia* **51**, 344–356 (2018).

134. M. J. Melchin, C. Holmden, Carbon isotope chemostratigraphy of the Llandovery in Arctic Canada: Implications for global correlation and sea-level change. *GFF* **128**, 173–180 (2006).

135. J. C. Gouldey, M. R. Saltzman, S. A. Young, D. Kaljo, Strontium and carbon isotope stratigraphy of the Llandovery (Early Silurian): Implications for tectonics and weathering. *Palaeogeogr. Palaeoclimatol. Palaeoecol.* **296**, 264–275 (2010).

136. D. Kaljo, V. Grytsenko, T. Martma, M. A. Mõtus, Three global carbon isotope shifts in the Silurian of Podolia (Ukraine): Stratigraphical implications. *Est. J. Earth Sci.* **56**, 205–220 (2007).

137. B. D. Cramer, D. K. Loydell, C. Samtleben, A. Munnecke, D. Kaljo, P. Männik, T. Martma, L. Jeppsson, M. A. Kleffner, J. E. Barrick, C. A. Johnson, P. Emsbo, M. M. Joachimski, T. Bickert, M. R. Saltzman, Testing the limits of Paleozoic chronostratigraphic correlation via high-resolution (¡500 k.y.) integrated conodont, graptolite, and carbon isotope ($\delta^{13}C_{carb}$) biochemostratigraphy across the Llandovery–Wenlock (Silurian)

boundary: Is a unified Phanerozoic time scale achievable? *Bull. Geol. Soc. Am.* **122**, 1700–1716 (2010).

138. A. V. Hess, J. M. Trop, Sedimentology and carbon isotope (δ^{13}C) stratigraphy of Silurian-Devonian boundary interval strata, Appalachian Basin (Pennsylvania, USA). *Palaios* **34**, 405–423 (2019).

139. B. D. Cramer, M. A. Kleffner, M. R. Saltzman, The Late Wenlock Mulde positive carbon isotope ($\delta^{13}C_{carb}$) excursion in North America. *GFF* **128**, 85–90 (2006).

140. M. R. Saltzman, Carbon isotope (δ^{13}C) stratigraphy across the Silurian-Devonian transition in North America: Evidence for a perturbation of the global carbon cycle. *Palaeogeogr. Palaeoclimatol. Palaeoecol.* **187**, 83–100 (2002).

141. N. E. Buenger McAdams, Integrated carbon isotope chemostratigraphy and conodont biostratigraphy of the midcontinent Silurian, and a new date for the Devonian 'Kalkberg' K-bentonite, Ph.D. thesis, University of Iowa (2016).

142. S. C. Oborny, B. D. Cramer, C. E. Brett, A. M. Bancroft, Integrated Silurian conodont and carbonate carbon isotope stratigraphy of the east-central Appalachian Basin. *Palaeogeogr. Palaeoclimatol. Palaeoecol.* **554** (2020).

143. C. B. Waid, B. D. Cramer, Global chronostratigraphic correlation of the Llandovery Series (Silurian System) in Iowa, USA, using high-resolution carbon isotope ($\delta^{13}C_{carb}$) chemostratigraphy and brachiopod and conodont biostratigraphy. *Bulletin of Geosciences* **92** (2017).

144. B. D. Cramer, M. R. Saltzman, Sequestration of ^{12}C in the deep ocean during the early Wenlock (Silurian) positive carbon isotope excursion. *Palaeogeogr. Palaeoclimatol. Palaeoecol.* **219**, 333–349 (2005).

145. W. Buggisch, U. Mann, Carbon isotope stratigraphy of Lochkovian to Eifelian limestones from the Devonian of central and southern Europe. *International Journal of Earth Sciences* **93**, 521–541 (2004).

146. D. Chen, H. Qing, R. Li, The Late Devonian Frasnian-Famennian (F/F) biotic crisis: Insights from δ13Ccarb, δ13 Corg and 87Sr/86Sr isotopic systematics. *Earth Planet. Sci. Lett.* **235**, 151–166 (2005).

147. L. Ferrová, J. Frýda, P. Lukeš, High-resolution tentaculite biostratigraphy and facies development across the Early Devonian Daleje Event in the Barrandian (Bohemia): Implications for global Emsian stratigraphy. *Bull. Geosci.* **87** (2012).

148. K. Hillbun, T. E. Playton, E. Tohver, K. Ratcliffe, K. Trinajstic, B. Roelofs, S. Caulfield-Kerney, D. Wray, P. Haines, R. Hocking, D. Katz, P. Montgomery, P. Ward, Upper Kellwasser carbon isotope excursion pre-dates the F-F boundary in the Upper Devonian Lennard Shelf carbonate system, Canning Basin, Western Australia. *Palaeogeogr. Palaeoclimatol. Palaeoecol.* **438**, 180–190 (2015).

149. J. Hladíková, J. Hladil, B. Kříbek, Carbon and oxygen isotope record across Pridoli to Givetian stage boundaries in the Barrandian basin (Czech Republic). *Palaeogeogr. Palaeoclimatol. Palaeoecol.* **132**, 225–241 (1997).

150. J. M. Husson, B. Schoene, S. Bluher, A. C. Maloof, Chemostratigraphic and U-Pb geochronologic constraints on carbon cycling across the Silurian-Devonian boundary. *Earth Planet. Sci. Lett.* **436**, 108–120 (2016).

151. O. P. Izokh, N. G. Izokh, V. A. Ponomarchuk, D. V. Semenova, Carbon and oxygen isotopes in the Frasnian-Famennian section of the Kuznetsk basin (southern West Siberia). *Russ. Geol. Geophys.* **50**, 610–617 (2009).

152. A. A. Makhnach, B. G. Pokrovsky, O. V. Murashko, O. L. Petrov, Carbon and Oxygen Isotopes and Formation Conditions of the Upper Famennian Shale-Bearing Rocks in the Pripyat Trough, Southern Belarus. *Lithol. Miner. Resour.* **55**, 24–35 (2020).

153. K. Małkowski, G. Racki, A global biogeochemical perturbation across the Silurian-Devonian boundary: Ocean-continent-biosphere feedbacks (2009).

154. J. R. Morrow, C. A. Sandberg, K. Malkowski, M. M. Joachimski, Carbon isotope chemostratigraphy and precise dating of middle Frasnian (lower Upper Devonian) Alamo Breccia, Nevada, USA. *Palaeogeogr. Palaeoclimatol. Palaeoecol.* **282**, 105–118 (2009).

155. A. C. da Silva, F. Boulvain, Carbon isotope lateral variability in a Middle Frasnian carbonate platform (Belgium): Significance of facies, diagenesis and sea-level history. *Palaeogeogr. Palaeoclimatol. Palaeoecol.* **269**, 189–204 (2008).

156. P. J. Van Hengstum, D. R. Gröcke, Stable isotope record of the Eifelian-Givetian boundary Kačák-otomari Event (Middle Devonian) from Hungry Hollow, Ontario, Canada. *Can. J. Earth Sci.* **45**, 353–366 (2008).

157. J. J. Zambito, C. E. Brett, G. C. Baird, The late middle Devonian (Givetian) Global Taghanic biocrisis in its type area (Northern Appalachian Basin): Geologically rapid faunal transitions driven by global and local environmental changes. *Earth Life Glob. Biodiversity, Extinction Intervals Biogeogr. Perturbations Through Time* (Springer Netherlands, 2012), pp. 677–703.

158. D. Zhang, Z. Tang, H. Huang, G. Zhou, C. Cui, Y. Weng, W. Liu, S. Kim, S. Lee, M. Perez-Neut, J. Ding, D. Czyz, R. Hu, Z. Ye, M. He, Y. G. Zheng, H. A. Shuman, L. Dai, B. Ren, R. G. Roeder, L. Becker, Y. Zhao, Metabolic regulation of gene expression by histone lactylation. *Nature* **574**, 575–580 (2019).

159. S. R. Cole, J. T. Haynes, P. C. Lucas, R. A. Lambert, Faunal and sedimentological analysis of a latest Silurian stromatoporoid biostrome from the central Appalachian Basin. *Facies* **61** (2015).

160. J. Liu, T. J. Algeo, W. Qie, M. R. Saltzman, Intensified oceanic circulation during Early Carboniferous cooling events: Evidence from carbon and nitrogen isotopes. *Palaeogeogr. Palaeoclimatol. Palaeoecol.* **531**, 108962 (2019).

161. D. Maharjan, G. Jiang, Y. Peng, R. A. Henry, Paired carbonate-organic carbon and nitrogen isotope variations in Lower Mississippian strata of the southern Great Basin, western United States. *Palaeogeogr. Palaeoclimatol. Palaeoecol.* **490**, 462–472 (2018).

162. L. S. Batt, I. P. Montañez, P. Isaacson, M. C. Pope, S. H. Butts, J. Abplanalp, Multi-carbonate component reconstruction of mid-carboniferous (Chesterian) seawater δ13C. *Palaeogeogr. Palaeoclimatol. Palaeoecol.* **256**, 298–318 (2007).

163. U. Brand, G. Jiang, K. Azmy, J. Bishop, I. P. Montañez, Diagenetic evaluation of a Pennsylvanian carbonate succession (Bird Spring Formation, Arrow Canyon, Nevada, U.S.A.) - 1: Brachiopod and whole rock comparison. *Chem. Geol.* **308-309**, 26–39 (2012).

164. W. Buggisch, X. Wang, A. S. Alekseev, M. M. Joachimski, Carboniferous–Permian carbon isotope stratigraphy of successions from China (Yangtze Platform), USA (Kansas) and Russia (Moscow Basin and Urals). *Palaeogeography, Palaeoclimatology, Palaeoecology* **301**, 18–38 (2011).

165. J. T. Koch, T. D. Frank, T. P. Bulling, Stable-isotope chemostratigraphy as a tool to correlate complex Mississippian marine carbonate facies of the Anadarko shelf Oklahoma and Kansas. *Am. Assoc. Pet. Geol. Bull.* **98**, 1071–1090 (2014).

166. A. G. Liu, C. G. Kenchington, E. G. Mitchell, Remarkable insights into the paleoecology of the Avalonian Ediacaran macrobiota (2015).

167. C. Liu, E. Jarochowska, Y. Du, D. Vachard, A. Munnecke, Stratigraphical and δ^{13}C records of Permo-Carboniferous platform carbonates, South China: responses to late Paleozoic icehouse climate and icehouse–greenhouse transition. *Palaeogeography, Palaeoclimatology, Palaeoecology* **474**, 113–129 (2017).

168. K. M. Meyer, M. Yu, D. Lehrmann, B. van de Schootbrugge, J. L. Payne, Constraints on Early Triassic carbon cycle dynamics from paired organic and inorganic carbon isotope records. *Earth Planet. Sci. Lett.* **361**, 429–435 (2013).

169. T. Galfetti, H. Bucher, A. Brayard, P. A. Hochuli, H. Weissert, K. Guodun, V. Atudorei, J. Guex, Late Early Triassic climate change: Insights from carbonate carbon isotopes, sedimentary evolution and ammonoid paleobiogeography. *Palaeogeogr. Palaeoclimatol. Palaeoecol.* **243**, 394–411 (2007).

170. G. Luo, T. J. Algeo, J. Huang, W. Zhou, Y. Wang, H. Yang, S. Richoz, S. Xie, Vertical $\delta^{13}C_{org}$ gradients record changes in planktonic microbial community composition during the end-Permian mass extinction. *Palaeogeogr. Palaeoclimatol. Palaeoecol.* **396**, 119–131 (2014).

171. A. Baud, V. Atudorei, Z. Sharp, Late permian and early triassic evolution of the northern indian margin: carbon isotope and sequence stratigraphy. *Geodin. Acta* **9**, 57–77 (1996).

172. Carbon and strontium isotope stratigraphy of the Permian from Nevada and China: Implications from an icehouse to greenhouse transition, author=Tierney, Kate E, year=2010, school=The Ohio State University, Ph.D. thesis.

173. W. Buggisch, K. Krainer, M. Schaffhauser, M. Joachimski, C. Korte, Late Carboniferous to Late Permian carbon isotope stratigraphy: A new record from post-Variscan carbonates from the Southern Alps (Austria and Italy). *Palaeogeography, Palaeoclimatology, Palaeoecology* **433**, 174–190 (2015).

174. C. Cheng, S. Li, X. Xie, T. Cao, W. L. Manger, A. B. Busbey, Permian carbon isotope and clay mineral records from the Xikou section, Zhen'an, Shaanxi Province, central China: climatological implications for the easternmost Paleo-Tethys. *Palaeogeography, Palaeoclimatology, Palaeoecology* **514**, 407–422 (2019).

175. K. T. Cramer, M. Bostic, High-resolution carbon isotope ($\delta^{13}C_{carb}$) chemostratigraphy of the lower Permian from the US midcontinent: Checking the pulse of the late Paleozoic ice age. *Bulletin* **127**, 584–595 (2015).

176. J. C. Laya, M. E. Tucker, D. R. Gröcke, A. Perez-Huerta, Carbon, oxygen and strontium isotopic composition of low-latitude Permian carbonates (Venezuelan Andes): climate proxies of tropical Pangea. *Geological Society, London, Special Publications* **376**, 367–385 (2013).

177. S.-z. Shen, C.-q. Cao, H. Zhang, S. A. Bowring, C. M. Henderson, J. L. Payne, V. I. Davydov, B. Chen, D.-x. Yuan, Y.-c. Zhang, *et al.*, High-resolution $\delta^{13}C_{carb}$ chemostratigraphy from latest Guadalupian through earliest Triassic in South China and Iran. *Earth and Planetary Science Letters* **375**, 156–165 (2013).

178. A. Bachan, B. van de Schootbrugge, J. Fiebig, C. A. McRoberts, G. Ciarapica, J. L. Payne, Carbon cycle dynamics following the end-Triassic mass extinction: Constraints from paired $\delta^{13}C_{carb}$ and $\delta^{13}C_{org}$ records. *Geochemistry, Geophysics, Geosystems* **13** (2012).

179. C. Korte, S. P. Hesselbo, H. C. Jenkyns, R. E. Rickaby, C. Spötl, Palaeoenvironmental significance of carbon- and oxygen-isotope stratigraphy of marine Triassic-Jurassic boundary sections in SW Britain. *J. Geol. Soc. London.* **166**, 431–445 (2009).

180. R. Morante, A. Hallam, Organic carbon isotopic record across the Triassic-Jurassic boundary in Austria and its bearing on the cause of the mass extinction. *Geology* **24**, 391–394 (1996).

181. M. Hermoso, F. Minoletti, R. E. Rickaby, S. P. Hesselbo, F. Baudin, H. C. Jenkyns, Dynamics of a stepped carbon-isotope excursion: Ultra high-resolution study of Early Toarcian environmental change. *Earth Planet. Sci. Lett.* **319-320**, 45–54 (2012).

182. S. P. Hesselbo, H. C. Jenkyns, L. V. Duarte, L. C. Oliveira, Carbon-isotope record of the Early Jurassic (Toarcian) Oceanic Anoxic Event from fossil wood and marine carbonate (Lusitanian Basin, Portugal). *Earth Planet. Sci. Lett.* **253**, 455–470 (2007).

183. N. Preto, C. Agnini, M. Rigo, M. Sprovieri, H. Westphal, The calcareous nannofossil Prinsiosphaera achieved rock-forming abundances in the latest Triassic of western Tethys: consequences for the δ^{13}C of bulk carbonate. *Biogeosciences* **10**, 6053–6068 (2013).

184. W. Xu, M. Ruhl, H. C. Jenkyns, M. J. Leng, J. M. Huggett, D. Minisini, C. V. Ullmann, J. B. Riding, J. W. Weijers, M. S. Storm, *et al.*, Evolution of the Toarcian (Early Jurassic) carbon-cycle and global climatic controls on local sedimentary processes (Cardigan Bay Basin, UK). *Earth and Planetary Science Letters* **484**, 396–411 (2018).

185. R. Aguado, L. O'Dogherty, J. Sandoval, Calcareous nannofossil assemblage turnover in response to the Early Bajocian (Middle Jurassic) palaeoenvironmental changes in the Subbetic Basin. *Palaeogeography, Palaeoclimatology, Palaeoecology* **472**, 128–145 (2017).

186. J. Grabowski, V. Bakhmutov, Š. Kdỳr, M. Krobicki, P. Pruner, D. Reháková, P. Schnabl, K. Stoykova, H. Wierzbowski, Integrated stratigraphy and palaeoenvironmental interpretation of the Upper Kimmeridgian to Lower Berriasian pelagic sequences of the Velykyi Kamianets section (Pieniny Klippen Belt, Ukraine). *Palaeogeography, Palaeoclimatology, Palaeoecology* **532**, 109216 (2019).

187. G. Muttoni, M. Mazza, D. Mosher, M. E. Katz, D. V. Kent, M. Balini, A Middle–Late Triassic (Ladinian–Rhaetian) carbon and oxygen isotope record from the Tethyan Ocean. *Palaeogeography, Palaeoclimatology, Palaeoecology* **399**, 246–259 (2014).

188. L. O'Dogherty, R. Aguado, P. O. Baumgartner, M. Bill, Š. Goričan, J. Sandoval, L. Sequeiros, Carbon-isotope stratigraphy and pelagic biofacies of the Middle–Upper Jurassic transition in the Tethys–Central Atlantic connection. *Palaeogeography, Palaeoclimatology, Palaeoecology* **507**, 129–144 (2018).

189. M. S. Storm, S. P. Hesselbo, H. C. Jenkyns, M. Ruhl, C. V. Ullmann, W. Xu, M. J. Leng, J. B. Riding, O. Gorbanenko, Orbital pacing and secular evolution of the Early Jurassic carbon cycle. *Proceedings of the National Academy of Sciences* **117**, 3974–3982 (2020).

190. X. Sun, T. Zhang, Y. Sun, K. L. Milliken, D. Sun, Geochemical evidence of organic matter source input and depositional environments in the lower and upper Eagle Ford Formation, south Texas. *Org. Geochem.* **98**, 66–81 (2016).

191. M. L. Gomes, M. T. Hurtgen, B. B. Sageman, Biogeochemical sulfur cycling during Cretaceous oceanic anoxic events: A comparison of OAE1a and OAE2. *Paleoceanography* **31**, 233–251 (2016).

192. J. S. Eldrett, C. Ma, S. C. Bergman, B. Lutz, F. J. Gregory, P. Dodsworth, M. Phipps, P. Hardas, D. Minisini, A. Ozkan, J. Ramezani, S. A. Bowring, S. L. Kamo, K. Ferguson,

C. Macaulay, A. E. Kelly, An astronomically calibrated stratigraphy of the Cenomanian, Turonian and earliest Coniacian from the Cretaceous Western Interior Seaway, USA: Implications for global chronostratigraphy. *Cretac. Res.* **56**, 316–344 (2015).

193. I. Jarvis, J. Trabucho-Alexandre, D. R. Gröcke, D. Uličný, J. Laurin, Intercontinental correlation of organic carbon and carbonate stable isotope records: evidence of climate and sea-level change during the Turonian (Cretaceous). *Depos. Rec.* **1**, 53–90 (2015).

194. J. O. Herrle, C. J. Schröder-Adams, W. Davis, A. T. Pugh, J. M. Galloway, J. Fath, Mid-Cretaceous high arctic stratigraphy, climate, and oceanic anoxic events. *Geology* **43**, 403–406 (2015).

195. J. A. Moreno-Bedmar, J. Sandoval, J. Tavera, T. Bover-Arnal, R. Salas, G. Delanoy, F.-M. Maurrasse, R. Martínez, *et al.*, Lower Aptian ammonite and carbon isotope stratigraphy in the eastern Prebetic Domain (Betic Cordillera, southeastern Spain). *Geologica Acta* **10**, 333–354 (2012).

196. A. M. Oehlert, P. K. Swart, Interpreting carbonate and organic carbon isotope covariance in the sedimentary record. *Nat. Commun.* **5** (2014).

197. B. J. Tipple, M. Pagani, S. Krishnan, S. S. Dirghangi, S. Galeotti, C. Agnini, L. Giusberti, D. Rio, Coupled high-resolution marine and terrestrial records of carbon and hydrologic cycles variations during the Paleocene-Eocene Thermal Maximum (PETM). *Earth Planet. Sci. Lett.* **311**, 82–92 (2011).

198. E. M. Crouch, G. R. Dickens, H. Brinkhuis, M. P. Aubry, C. J. Hollis, K. M. Rogers, H. Visscher, The Apectodinium acme and terrestrial discharge during the Paleocene-Eocene thermal maximum: New palynological, geochemical and calcareous nannoplank-

ton observations at Tawanui, New Zealand. *Palaeogeogr. Palaeoclimatol. Palaeoecol.* **194**, 387–403 (2003).

199. A. Montanari, K. Farley, P. Claeys, D. De Vleeschouwer, N. De Winter, S. Vansteenberge, M. Sinnesael, C. Koeberl, Stratigraphic record of the asteroidal Veritas breakup in the Tortonian Monte dei Corvi section (Ancona, Italy). *Bulletin* **129**, 1357–1376 (2017).

200. N. Anderson, J. R. Kelson, S. Kele, M. Daëron, M. Bonifacie, J. Horita, T. J. Mackey, C. M. John, T. Kluge, P. Petschnig, A. Jost, K. Huntington, S. Bernasconi, K. Bergmann, A unified clumped isotope thermometer calibration (0.5–1,100 C) using carbonate-based standardization. *Geophysical Research Letters* **48**, e2020GL092069 (2021).

201. J. P. Pu, S. A. Bowring, J. Ramezani, P. Myrow, T. D. Raub, E. Landing, A. Mills, E. Hodgin, F. A. Macdonald, Dodging snowballs: Geochronology of the Gaskiers glaciation and the first appearance of the Ediacaran biota. *Geology* **44**, 955–958 (2016).

202. J. L. Isbell, F. F. Vesely, E. L. Rosa, K. N. Pauls, N. D. Fedorchuk, L. R. Ives, N. B. McNall, S. A. Litwin, M. K. Borucki, J. E. Malone, *et al.*, Evaluation of physical and chemical proxies used to interpret past glaciations with a focus on the late Paleozoic Ice Age. *Earth-Science Reviews* **221**, 103756 (2021).

203. B. H. Passey, N. E. Levin, T. E. Cerling, F. H. Brown, J. M. Eiler, K. K. Turekian, High-temperature environments of human evolution in East Africa based on bond ordering in paleosol carbonates. *Proc. Natl. Acad. Sci. U. S. A.* **107**, 11245–11249 (2010).

204. K. W. Huntington, J. M. Eiler, H. P. Affek, W. Guo, M. Bonifacie, L. Y. Yeung, N. Thiagarajan, B. Passey, A. Tripati, M. Daëron, R. Came, Methods and limitations of 'clumped' CO_2 isotope (Δ_{47}) analysis by gas-source isotope ratio mass spectrometry. *J. Mass Spectrom.* **44**, 1318–1329 (2009).

205. S. M. Bernasconi, M. Daëron, K. D. Bergmann, M. Bonifacie, A. N. Meckler, H. P. Affek, N. Anderson, D. Bajnai, E. Barkan, E. Beverly, *et al.*, InterCarb: A community effort to improve interlaboratory standardization of the carbonate clumped isotope thermometer using carbonate standards. *Geochemistry, Geophysics, Geosystems* **22**, e2020GC009588 (2021).

206. S. M. Bernasconi, I. A. Müller, K. D. Bergmann, S. F. Breitenbach, A. Fernandez, D. A. Hodell, M. Jaggi, A. N. Meckler, I. Millan, M. Ziegler, Reducing uncertainties in carbonate clumped isotope analysis through consistent carbonate-based standardization. *Geochemistry, Geophysics, Geosystems* **19**, 2895–2914 (2018).

207. A. J. Schauer, J. Kelson, C. Saenger, K. W. Huntington, Choice of ^{17}O correction affects clumped isotope (Δ_{47}) values of CO_2 measured with mass spectrometry. *Rapid Commun. Mass Spectrom.* **30**, 2607–2616 (2016).

208. M. Daëron, D. Blamart, M. Peral, H. P. Affek, Absolute isotopic abundance ratios and the accuracy of Δ_{47} measurements. *Chem. Geol.* **442**, 83–96 (2016).

209. C. M. John, D. Bowen, Community software for challenging isotope analysis: First applications of 'Easotope' to clumped isotopes. *Rapid Commun. Mass Spectrom.* **30**, 2285–2300 (2016).

210. P. K. Swart, S. J. Burns, J. J. Leder, Fractionation of the stable isotopes of oxygen and carbon in carbon dioxide during the reaction of calcite with phosphoric acid as a function of temperature and technique. *Chem. Geol. Isot. Geosci. Sect.* **86**, 89–96 (1991).

211. J. Rosenbaum, S. M. F. Sheppard, An isotopic study of siderites, dolomites and ankerites at high temperatures. *Geochim. Cosmochim. Acta* **50**, 1147–1150 (1986).

212. M. Daëron, Full propagation of analytical uncertainties in $\Delta 47$ measurements. *Geochemistry, Geophysics, Geosystems* **22**, e2020GC009592 (2021).

213. K. J. Dennis, H. P. Affek, B. H. Passey, D. P. Schrag, J. M. Eiler, Defining an absolute reference frame for "clumped" isotope studies of CO_2. *Geochim. Cosmochim. Acta* **75**, 7117–7131 (2011).

214. T. Coplen, Calibration of the calcite–water oxygen-isotope geothermometer at Devils Hole, Nevada, a natural laboratory. *Geochim. Cosmochim. Acta* **71**, 3948–3957 (2007).

215. J. Horita, Oxygen and carbon isotope fractionation in the system dolomite–water–CO_2 to elevated temperatures. *Geochim. Cosmochim. Acta* **129**, 111–124 (2014).

216. A. Matthews, A. Katz, Oxygen isotope fractionation during the dolomitization of calcium carbonate. *Geochim. Cosmochim. Acta* **41**, 1431–1438 (1977).

217. C. Vasconcelos, J. A. McKenzie, R. Warthmann, Calibration of the δ^{18}O paleothermometer for dolomite precipitated in microbial cultures and natural environments. *Geology* (2005).

218. E. Grosjean, G. D. Love, C. Stalvies, D. A. Fike, R. E. Summons, Origin of petroleum in the Neoproterozoic-Cambrian South Oman Salt Basin. *Org. Geochem.* **40**, 87–110 (2009).

219. G. D. Love, E. Grosjean, C. Stalvies, D. A. Fike, J. P. Grotzinger, A. S. Bradley, A. E. Kelly, M. Bhatia, W. Meredith, C. E. Snape, S. A. Bowring, D. J. Condon, R. E. Summons, Fossil steroids record the appearance of Demospongiae during the Cryogenian period. *Nature* **457**, 718–721 (2009).

220. M. K. Lloyd, U. Ryb, J. M. Eiler, Experimental calibration of clumped isotope reordering in dolomite. *Geochim. Cosmochim. Acta* **242**, 1–20 (2018).

221. M. K. Lloyd, J. M. Eiler, P. I. Nabelek, Clumped isotope thermometry of calcite and dolomite in a contact metamorphic environment. *Geochim. Cosmochim. Acta* **197**, 323–344 (2017).

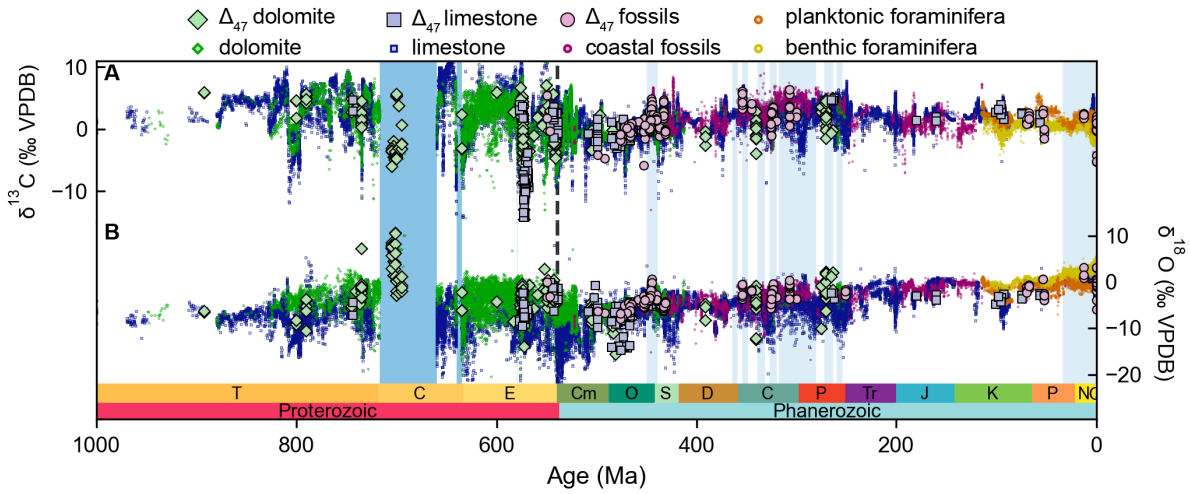

Fig. 1. Carbonate mineral δ^{13}C and δ^{18}O values through the last 1 Ga (**A**) δ^{13}C of limestone rocks (blue squares), dolomite rocks (green diamonds), shallow marine coastal fossils (purple circles), planktonic foraminifera (orange circles), benthic foraminifera (yellow circles), and Δ_{47} samples (lighter colors with black outlines, same symbols). (**B**) δ^{18}O values with same symbology as above. Vertical bars indicate events: two Snowball Earth glaciations (dark blue), high latitude glaciations (light blue), and the Neoproterozoic–Phanerozoic boundary (dashed black line). See (*30*) for included data and age constraints on glaciations..

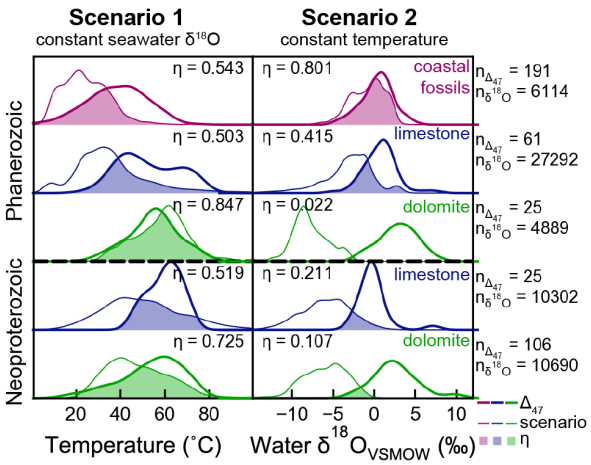

Fig. 2. A comparison of Scenario 1 vs. Δ_{47}-temperature and Scenario 2 vs. Δ_{47}-derived water $\delta^{18}O_{VSMOW}$ (**A**) Scenario 1 assumes mineral δ^{18}O depends on temperature using a water $\delta^{18}O_{VSMOW}$ value of $-1.2‰$ and higher values during glacial intervals to calculate temperature (*30*). Shallow marine fossil (purple), and Phanerozoic and Neoproterozoic limestone rock (blue), and dolomite (green) Gaussian kernel density estimates of δ^{18}O translated under the assumptions of Scenario 1 (thin line) compared to Phanerozoic fossil Δ_{47}-temperature (thick line). The overlap η is the fraction of the distributions that overlay each other. It is estimated as the area under the minimum of the distributions along the curves. The number of samples used in each KDE is to the right of the plot. (**B**) Scenario 2 assumes the mineral δ^{18}O increase depends only on changing seawater δ^{18}O. Seawater temperature is held at a constant 25°C to calculate seawater δ^{18}O (*30*). Phanerozoic and Neoproterozoic Gaussian kernel density estimates of δ^{18}O translated under the assumptions of Scenario 2 (thin line) compared to Δ_{47}-derived water $\delta^{18}O_{VSMOW}$(thick line). Clumped data used in Fig.2 is $\leq$75°C.

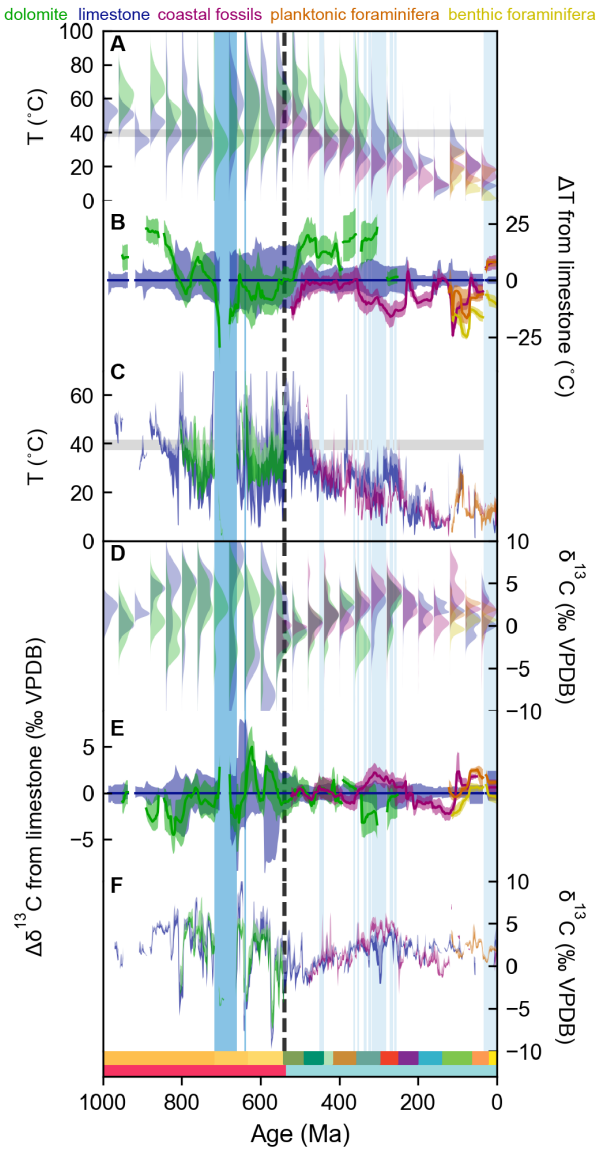

Fig. 3. Temperature and δ^{13}C temporal variability by material. (**A,D**) Distribution of temperature estimates from Scenario 1 and δ^{13}C for limestone rocks (blue), dolomite rocks (green), shallow marine coastal fossils (purple), planktonic foraminifera (orange), and benthic foraminifera (yellow). (**B,E**) dolomite and coastal fossil lines are the difference of their respective medians from the limestone median (zero) for temperature (B) and δ^{13}C (E). The shaded envelopes are the difference of the 25th and 75th quantiles from the limestone median.

(**C**) The 1^{st} to 50$^{\text{th}}$ quantiles of Scenario 1 temperature for shallow marine fossils, planktonic foraminifera, limestone and Neoproterozoic dolomite (538.8$\leq$ DL $\leq$805 Ma). No dolomite in the Phanerozoic and early Neoproterozoic is included. The 1$^{\text{st}}$ quartile is approximated using the 1$^{\text{st}}$ to 25^{th} quantiles and is darker than the 2$^{\text{nd}}$. (**F**) The median of δ^{13}Cvalues, with a shaded envelope from the 25 to 75$^{\text{th}}$ quantiles. Dolomite is excluded as in (C). The distributions in Fig. 3A,D and the moving distributions in Fig. 3B,E are generated using Gaussian kernel density estimates as above with window of 40 Myr. Windows with fewer than 14 points are excluded. The moving distributions are sampled each 2 Myr. The moving quartiles in Fig. 3C,F are estimated using quantile regression on points within 4 Myr windows sampled each 2 Myr. Vertical bars indicate events: two Snowball Earth glaciations (dark blue), high latitude glaciations (light blue), and the Neoproterozoic–Phanerozoic boundary (dashed black line) (*30*).

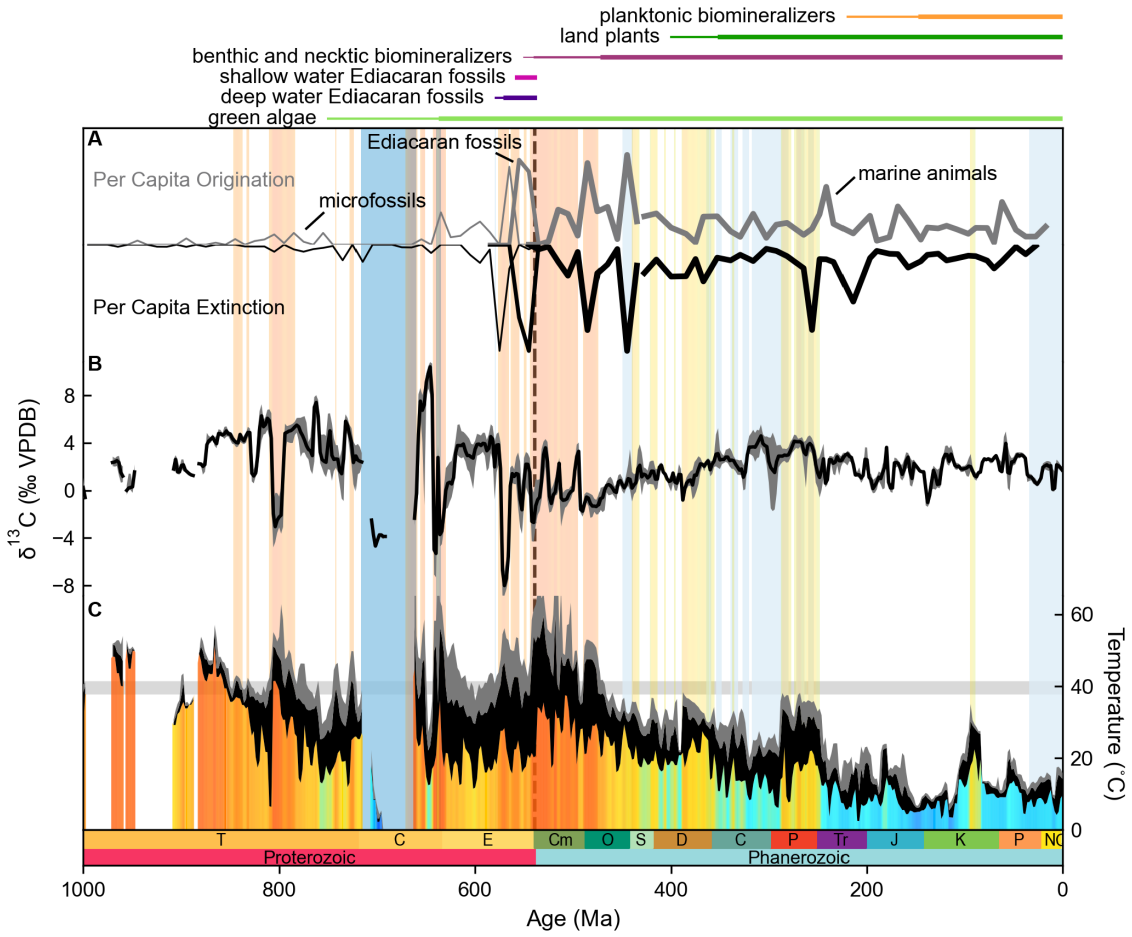

Fig. 4. Critical extinction and origination events in the history of life, δ^{13}C, and a tropical marine temperature record (**A**) Scaled per capita origination and extinction rates are calculated in 10 Myr bins from occurrences of Neoproterozoic microfossils (thin line) (*60–62*), macroscopic Ediacaran fauna (medium line) (*63*), Cambrian and Ordovician fossil marine genera (*57*), and Ordovician through modern fossil marine genera (*59*) using (*58, 74*)(see (*30*)). Ordovician through modern occurrences are subsampled using classical rarefaction and the R DivDyne package. (**B**) The composite δ^{13}C record is plotted as in Fig. 3F with the 2^{nd} and 3^{rd} quartiles (grey) and median (black). (**C**) The composite temperature record is plotted as in Fig. 3C using the 1^{st} (black) and 2^{nd} quartiles (grey) and a color bar. The horizontal grey band

represents the upper thermal limit for modern tropical subtidal ectotherms (*75*). Vertical bars indicate two Snowball Earth glaciations (dark blue), high latitude glaciations (light blue), and the Neoproterozoic–Phanerozoic boundary (dashed black line). Before 440 Ma, intervals $\geq$1 Myr with a 25$^{\text{th}}$ quantile temperature $\geq$ 38°C are extended to the top of the plot (orange vertical bars). After 440 Ma, the threshold is $\geq$ 28°C (green and yellow vertical bars).

Supplementary Materials for: A billion years of temperature variability: a key driver of Earth's long-term habitability

Authors:

Kristin D. Bergmann, Nicholas Boekelheide, Julia W. Clarke,

Marjorie D. Cantine, Julia Wilcots, Noah T. Anderson,

Adam B. Jost, Olivia Laub, Juliana Drozd, Samuel L. Goldberg,

Tyler Mackey, Fran Meyer, Athena Eyster

1 Materials and Methods

Mineral δ^{18}O compilation A literature search was conducted to locate published mineral δ^{18}O data from shallow platform carbonates spanning 1.5 Ga to the modern. Most of this data was associated with high-resolution δ^{13}C studies, usually sampled at meter-resolution. The δ^{18}O data from these individual studies of bulk rock δ^{13}C had not been previously compiled in a systematic way with a high-resolution age model. Study level isotopic datasets from the literature were digitized into .csv files, and metadata were added (location, mineralogy, type of material, Formation name, etc.).

Data included in mineral δ^{18}O compilation :

Mesoproterozoic: (*25, 76–81*)

Neoproterozoic: (*14, 24, 25, 82–103*)

Cambrian: (*85, 104–112*)

Ordovician: (*104, 107, 109, 113–131*)

Silurian: (*132–144*)

Devonian: (*138, 140, 145–159*)

Carboniferous: (*160–167*)

Permo-Triassic: (*164, 167–177*)

Triassic-Jurassic: (*178–190*)

Cretaceous: (*191–195*)

Cenozoic: (*196–199*)

Fossils: (*5, 6, 16*) with only tropical/subtropical used

Δ_{47} compilation Carbonate Δ_{47} data was compiled from (*12–14, 19, 20, 34, 35*) and references therein. Results in (*19*) were screened to remove all Arctic and Antarctic carbonates and all Cretaceous Interior Seaway carbonates to provide the best constraints on marine, tropical carbonate platforms through time. Results from (*12–14, 35*) are recalculated using the original raw voltage data into the I-CDES reference frame and a universal temperature calibration equation (*200*), whereas measurements from (*19, 20*) were not recalculated into the I-CDES or updated to the universal temperature calibration equation. We estimate this may affect temperatures by $\sim$5°C or less and will not alter the results in Fig. 2.

Age Model We created a consistent age model for all individual studies and opted not to use previously published age models individual authors may have created. In the Phanerozoic, we used the Geologic Time Scale 2020 to set period, epoch, stage, and sub-stage boundaries (*22*). Regional stage boundaries were used where applicable. We also used the GTS2020 to add additional tie points based on biostratigraphy (i.e., trilobite, conodont, and graptolite zones) and δ^{13}C excursions. Age models were built using information provided within the datasets, stratigraphic columns, and text of compiled articles. At the upper and lower boundaries of datasets when no other tie point could be found, the midpoint between the nearest tie point within the section and the next closest geologic stage was used as an estimated age tie point. For all points in the dataset, ages were interpolated using a linear model assuming a constant

sedimentation rate between tie points. Sedimentation rates were error checked for consistency. The age model for compiled δ^{18}O Proterozoic datasets utilized U/Pb and Re/Os ages from the published literature (*23–25, 51*) and δ^{13}C excursions were used to build a new age model for each study.

Scenario 1 and 2 calculations We have gathered mineralogical information for all samples in the δ^{18}O compilation so that we can explore the implications of Scenario 1 and Scenario 2. This mineralogical information was collected from stratigraphic columns and data tables. For Scenario 1 we calculated temperature using a water $\delta^{18}O_{VSMOW}$ value of $-1.2‰$(Scenario 1) except during known glacial intervals. For Scenario 2 we calculated water δ^{18}O using T = 25°CẆe used mineral-specific fractionation factors for calcite samples (*26*) and dolomite samples (*27*). Ice volume estimates for Scenario 1 are as follows: [717–660 Ma],[640–630 Ma],[450–439 Ma]: $\delta^{18}O_{VSMOW}$ value of $0‰$. [317.5–280 Ma],[33.9–0 Ma]: $\delta^{18}O_{VSMOW}$ value of $-0.5‰$. [580–579 Ma],[364–359 Ma],[354–348.5 Ma],[339–331.5 Ma],[327–320 Ma],[272–263.5 Ma],[259.5–254 Ma]: $\delta^{18}O_{VSMOW}$ value of $-0.8‰$. Ages of glacial intervals are from (*5, 35, 51, 201, 202*). The distributions in Fig. 2 are generated on the unweighted points using Gaussian kernel density estimates as implemented in the scipy package in python with bandwidth selected using Scott's Rule. The overlap η is the fraction of the distributions that overlay each other. It is estimated as the area under the minimum of the distributions along the curves. Material specific distributions for Scenario 1 are shown in Fig. 3A,D and the moving distributions in Fig. 3B,E are generated using Gaussian kernel density estimates with a window of 40 Myr. Windows with fewer than 14 points are excluded. The moving distributions are sampled each 2 Myr. The moving quartiles in Fig. 3C,F are estimated using quantile regression on points within 4 Myr windows sampled each 2 Myr. The first quartile is approximated using the 1^{st} to 25^{th} quantiles, and the fourth quartile is approximated using the 75^{th} to 99^{th}. Only

the 1^{st} and 2^{nd} quartiles (1^{st} to 50^{th} quantiles) are shown in Fig. 3C and Fig. 4C. All of the quartiles are shown as Scenario 1 and 2 in Fig. S1.

Per Capita Extinction and Origination Rates To calculate post-Ordovician Phanerozoic extinction and origination rates we used the R package DivDyn and used the data and code from (*58, 59*). This uses a Paleobiology Database download of marine animals. It resamples using stage level or 10 Myr bins and compares a variety of approached to calculate extinction and origination rates. We opt to plot the resampled dataset that uses classical rarefaction (CR) and per capita extinction and origination rates(PC) (*74*) in 10 Myr bins to best match the treatment of the sparser datasets described below. For older time intervals, We first calculated FAD and LAD from occurrences we tabulated for Neoproterozoic microfossils from (*60–62*), Neoproterozoic Ediacaran fauna from (*63*), and Cambrian and Ordovician marine fossil raw occurrence data from (*57*). We calculate per capita extinction and origination rates (*74*) on these three compilations using 10 Myr bins without subsampling. The age constraints we used for fossil occurrences in the Neoproterozoic are included in a Supplemental Table and in the OSF repository. Results are normalized to the largest per capita extinction or origination rate in each of the four records.

Materials for new Δ_{47} analyses All new samples presented are dolomite and were provided by Andrew Knoll. Three samples are from the Kotuikan Formation in the Anbar Uplift, Siberia (KG_92_21, KG_92_24, KG_92_27B, plotted at 1450 Ma), Five samples are from the Dismal Lakes Group in N.W.T. (DL_2_B, DL_1_B, DL_1_A, DL_1_D, DL_2_A, plotted at 1300 Ma). Five samples are from the Svanbergfjellet Formation, Svalbard (G3_129f_A, G3129f_B,G3_135.6, G3_157.2_B, G3_157.2_A, plotted at 780 Ma). Four samples are from the Thule Group, NW Greenland (KS_78_12A, KS_78_12_B, KS_78_22, KS_78_7, plotted at 1150 Ma). Three samples are from the Wynniatt Formation and Reynolds Point Formation, Shaler

Group (88_KL_119, 88_KL_68_A, 88_KL_100, 88_KL_68_B, 88_KL_108_B, 88_KL_108_A, plotted at 802 Ma and 830 Ma respectively). Three samples are from the Pendjari Supergroup, Volta Basin, Burkina Faso (PK99_KT_4c_A, PK99_KT_3A, PK99_KT4C_B, plotted at 635 Ma).

Methods for new Δ_{47} analyses Precambrian samples described above were analyzed at the MIT Carbonate Research Lab on a Nu Perspective dual-inlet isotope ratio mass spectrometer coupled to a NuCarb automated sample preparation unit held at 70°CȦpproximately 450 μg of sample powder was weighed for each replicate from drilled polished sample slabs and digested in sample vials with 150 μL 104% phosphoric acid (H_3PO_4). Four or more replicates were analyzed per sample. Evolved CO_2 was purified cryogenically and by passage through a PorapakQ trap (1/4" inner diameter tube filled with 0.4 g 50-80 mesh PorapakQ bracketed by silver wool) held at -30°C. After purification, evolved CO_2 was transferred to a cold finger in a microvolume and warmed to room temperature. Reference gas pressure was balanced to match the sample beam size. Beam intensities were collected in three blocks of 20 integration cycles of 20 seconds each. Voltage on the m/z 44 beam at the start of each analysis is 8–20 V; this depleted by approximately 50% over a replicates analysis. Laboratory protocols for the distribution of standards throughout the 50-vial carousel changed over the course of this study. Prior to February 2018, queues were planned for $>$18 ETH standards alongside in-house standards and $<$23 unknown samples; after this point, 22 ETH standards were included in each run, along with three additional standards (IAEA-C1, IAEA-C2, and MERCK) and 25 unknowns. Uncommon shorter runs (i.e. $<$50 vials) exceeded the 1:1 sample:standard ratio.

All of the new Precambrian samples were also analyzed 1-2 times at Caltech in 2015. Methods follow those outlined in (*13*). Samples of 9–12 mg of powder were weighed into silver capsules before being reacted in a phosphoric common acid bath ($\sim 103\%; 1.90 \leq \rho \leq 1.92$) for 20 minutes at 90°C. Evolved CO_2 was collected and purified with an automated acid diges-

tion and gas purification device as described by (*203*). This device includes passing the CO_2 through multiple cryogenic traps using either a dry ice and ethanol mix or liquid nitrogen as well as through a Porapak-Q 120/80 mesh gas chromatography column held at $-20°C$ using a helium carrier gas. Sulfur was scrubbed from the CO_2 using an in-line silver wool trap. The CO_2 was measured on the ThermoFinnigan MAT 253 IRMS, nicknamed 'Admiral' housed at Caltech. Each measurement consisted of eight acquisitions (16V on m/z = 44) of seven cycles of unknown sample CO_2 versus Oztech working gas as outlined by (*204*). Best practices in the clumped isotope community have evolved to better address pressure baseline issues, non-linearity in the source, scale compression, and necessary sample replication (e.g., (*205–208*). We input raw measurement files of 1000°C heated and 25°C equilibrated gases and carbonate standard data along with raw measurement files of sample unknowns into Easotope, an open-source software tool specifically developed for clumped isotope data processing (*209*). The carbonate $\delta^{18}O$ values were calculated using a 90°C acid-digestion fractionation factor for calcite from (*210*) and for dolomite (*211*).

I-CDES transfer, temperature and water $\delta^{18}O$ calculations for all Δ_{47} analyses Both newly generated data (above) and previously published datasets generated by this studies' authors (*12–14, 21, 35*) were treated in an identical way and all datasets are standardized to I-CDES. All clumped isotope transformations used the raw d44, d45, d46, d47, d48, d49 measurements and sessions as output from Easotope to create an input file for ClumpyCrunch which propagates full error including uncertainty associated with the reference frame (*212*). For datasets generated at MIT, carbonate standards (ETH-1, ETH-2, ETH-3, ETH-4, IAEA-C2, and Merck) were used to transfer Δ_{47} values to the Intercarb Carbon Dioxide Equilibrium Scale (I-CDES) (*205, 213*) using anchor values from the InterCarb interlaboratory comparison project (*205*). For previously published datasets from Caltech, Δ_{47} values and temperatures

were recalculated into the I-CDES reference frame using a combination of anchors related to the above carbonate standards and the I-CDES reference frame: heated and equilibrated gases and HCM, CIT, TV01, TV03, TV04, 102-GZ-AZ-01 standards. These later anchors were re-measured at MIT and run through ClumpyCrunch using the I-CDES anchors ETH-1, ETH-2, ETH-3, ETH-4, IAEA-C2, and Merck. Total new analyses for each are standard are HCM [13], CIT [11], TV01 [recalculated from 272 Caltech analyses], TV03 [recalculated from 32 Caltech analyses], TV04 [11], and 102-GZ-AZ-01 [17] and nominal values in the I-CDES reference frame are in the legacy standard data file on OSF(link). The standards IAEA-C1, Fast Haga, 2-8-E, Carmel Chalk, and NCM were used to assess the data processing procedures. All code, nominal values, data evaluation plots, raw values and output for the ClumpyCrunch and BLIMP processing is available on OSF(link) and uses code outlined in (*200*). Final Δ_{47} temperatures were calculated using the calibration equation of (*200*). Δ_{47}-derived water δ^{18}O were calculated using the calcite-water fractionation equation from (*200*) which is similar to (*214*), but with more data, and (*215*) for dolomite in Fig. 2 and Fig. S1. Results from different water $\delta^{18}O_{VSMOW}$ fractionation equations are compared for calcite (*26, 200*) and for dolomite from (*215–217*) in the summary data file on OSF(link). Marine samples from other Phanerozoic compilations of calcite fossils and limestone (*19, 34*) and dolomite Δ_{47}-temperatures (*20*) are included but are not updated to I-CDES.

2 Supplemental Materials

Solid-state reordering and elevated Δ_{47}-temperatures We are undoubtedly presenting Δ_{47}-temperatures that have experienced solid state reordering in the compilation, particularly from Precambrian strata. Solid-state reordering would result in "apparent" enriched water δ^{18}O compositions. Thus, one could argue if all of our Precambrian samples have experienced significant solid state reordering, we have no basis for assessing seawater δ^{18}O through time. We think

the lower clumped isotope temperatures (¡75°C) from our data set merit consideration for the following reasons: [1] Δ_{47}-temperature results are from six different Precambrian carbonate platforms selected for their minimal to moderate burial histories, some of which yield intact biomarkers (*218, 219*). It is unlikely that all of these locations experienced similar degrees of solid state reordering. [2] Multiple samples throughout the record approach or sit at water δ^{18}O composition of -1.2‰ including bulk rock samples from both the Phanerozoic and Precambrian indicating bulk rocks can lithify early, record seawater $\delta^{18}O_{VSMOW}$ values, and preserve them for hundreds of millions of years, [3] Almost all of the Precambrian samples are dolomite which has been shown to be more resistant to solid state reordering than calcite (*220, 221*), [4] Our Δ_{47} results in multiple locations (both in the Phanerozoic and Precambrian (*12–14, 35*)) suggest that populations of carbonates in carbonate platforms often lithify in the presence of minimal fluids (i.e. sediment-buffered diagenesis where the pore fluids become buffered by the carbonate rocks and new fluids are not introduced) which lends more plausibility to interpreting the bottom of the distribution of both the δ^{18}O and Δ_{47}-derived water $\delta^{18}O_{VSMOW}$ results as a near primary record, [5] cold Δ_{47}-temperatures and heavy δ^{18}O values are preserved during glacial intervals (*13, 14, 21*). In summary, we have found Δ_{47} is more easily altered by lithification, subsequent post-depositional alteration, and solid state reordering than mineral δ^{18}O but not so much that the lowest preserved temperature populations loose all significance for interpreting primary environmental conditions in many shallowly buried locations. Both the Δ_{47} and δ^{18}O records preserve stratigraphic trends that suggest long-term (and shorter term) temperature fluctuations.

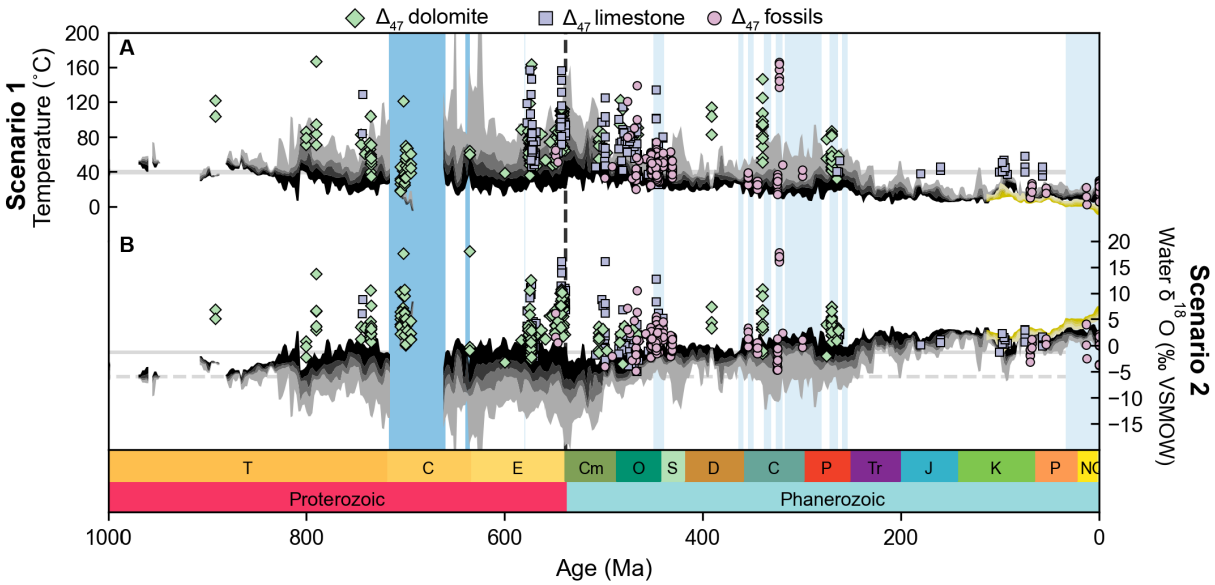

Fig. S1. Scenario 1 and Scenario 2 compared to Δ_{47}-temperature and Δ_{47}-derived water $\delta^{18}O_{VSMOW}$ values (**A**) Scenario 1 assumes mineral δ^{18}O depends primarily on temperature. Seawater $\delta^{18}O_{VSMOW}$ is held at a constant value of $-1.2‰$except during known glacial intervals (*30*) to calculate temperature (*27, 200*). Δ_{47}-temperature values (larger symbols) are compared to Scenario 2. Results are plotted as quartiles using the 1^{st} to 99^{th} quantiles of a moving distribution sampling each 1 Ma with a window of 5 Ma. The horizontal grey band represents the upper thermal limit for modern tropical subtidal ectotherms (*75*). (**B**) Scenario 2 assumes the mineral δ^{18}O increase depends primarily on changing seawater δ^{18}O. Seawater temperature is held at a constant 25°C to calculate seawater δ^{18}O (*27, 200*). Horizontal line indicates $-1.2‰$ seawater expected from Cenozoic ice-free conditions (*28, 29*). Results are plotted as quantiles of a moving distribution sampling each 1 Ma with a window of 5 Ma. Δ_{47}-derived water $\delta^{18}O_{VSMOW}$values (*27, 200*) are compared to Scenario 2 (larger symbols). Vertical light blue boxes indicate periods of glaciation. Dolomite rocks (green diamonds), limestone rocks (blue squares), and calcite, aragonite and apatite fossils (purple circles).

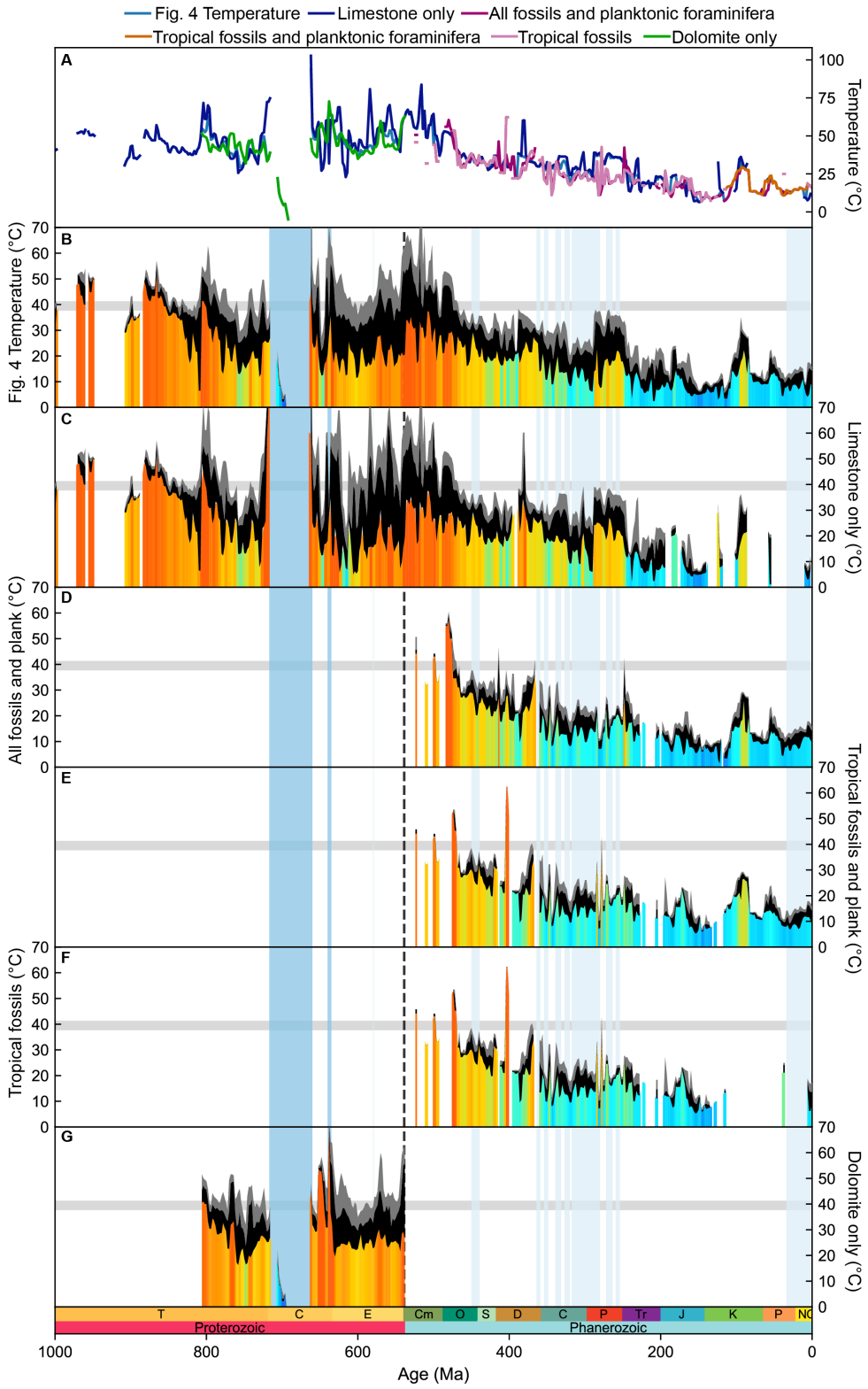
Fig. 4 Temperature
Limestone only
All fossils and planktonic foraminifera
Tropical fossils and planktonic foraminifera
Tropical fossils
Dolomite only
A
B
C
D
E
F
G
Temperature (°C)
Fig. 4 Temperature (°C)
Limestone only (°C)
All fossils and plank (°C)
Tropical fossils and plank (°C)
Tropical fossils (°C)
Dolomite only (°C)
T
C
E
Cm
O
S
D
C
P
Tr
J
K
P
Proterozoic
Phanerozoic
1000
800
600
400
200
0
Age (Ma)

Fig. S2. Individual components of the composite temperature record presented in Fig. 4C. (**A**) Temperature comparison of records in Fig. S2B,C,D,E,F. (**B**) The 1^{st} to 25^{th} quantiles (black) and 25th to 50th quantiles (grey) of shallow marine temperatures from Scenario 1 estimated using quantile regression on points within 4 Myr windows sampled each 2 Myr. (**B**) Scenario 1 temperatures derived from limestone samples. (**C**) Temperatures derived from coastal fossils and planktonic foraminifera. (**D**) Temperatures derived from tropical coastal fossils and tropical planktonic foraminifera, excluding all subtropical data. (**E**) Temperatures derived from tropical coastal fossils, excluding all planktonic foraminifera and subtropical fossil data. (**F**) Temperatures derived from Neoproterozoic dolomite ($\geq$805 Ma and $\leq$538.8 Ma). Grey bands represent the upper temperature limit of modern tropical subtidal ectotherms (*75*). Vertical bars indicate two Snowball Earth glaciations (dark blue), high latitude glaciations (light blue), and the Neoproterozoic–Phanerozoic boundary (dashed black line).

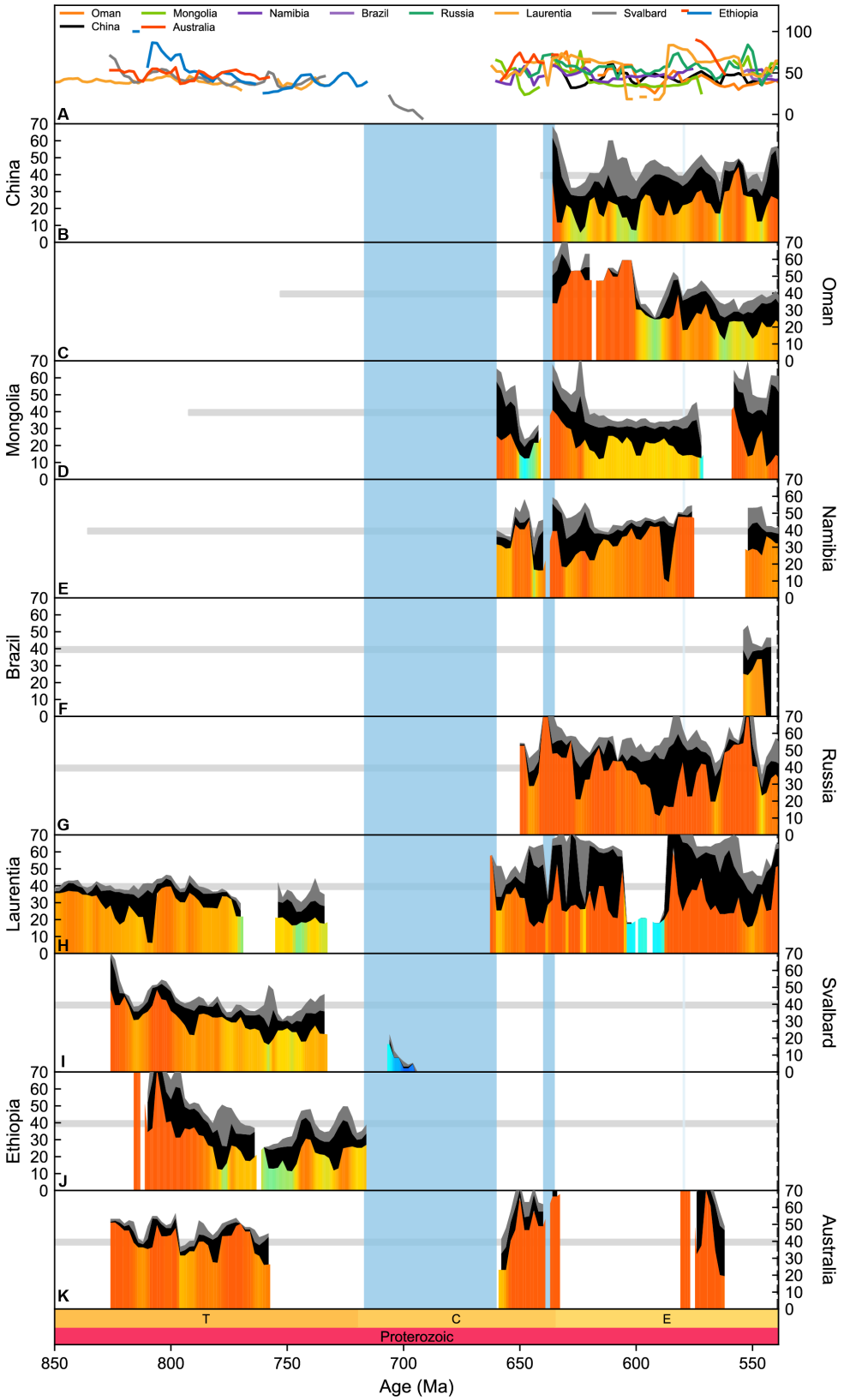
Oman
China
Mongolia
Australia
Namibia
Brazil
Russia
Laurentia
Svalbard
Ethiopia
A
B
C
D
E
F
G
H
I
J
K
T
C
E
Proterozoic
850
800
750
700
650
600
550
Age (Ma)

Fig. S3. Neoproterozoic country-level contributions to the composite temperature record presented in Fig. 4C. (**A**) Temperature comparison of the different countries. (**B-K**) The 1^{st} to 25^{th} quantiles (black) and 25th to 50th quantiles (grey) of shallow marine temperatures from Scenario 1 estimated using quantile regression on points within 4 Myr windows sampled each 2 Myr. In panel order, data are plotted from China, Oman, Mongolia, Namibia, Brazil, Russia, Laurentia (USA and Canada), Svalbard, Ethiopia, and Australia. Grey bands represent the upper temperature limit of modern tropical subtidal ectotherms (*75*). Vertical bars indicate two Snowball Earth glaciations (dark blue) and one high latitude glaciation (light blue).

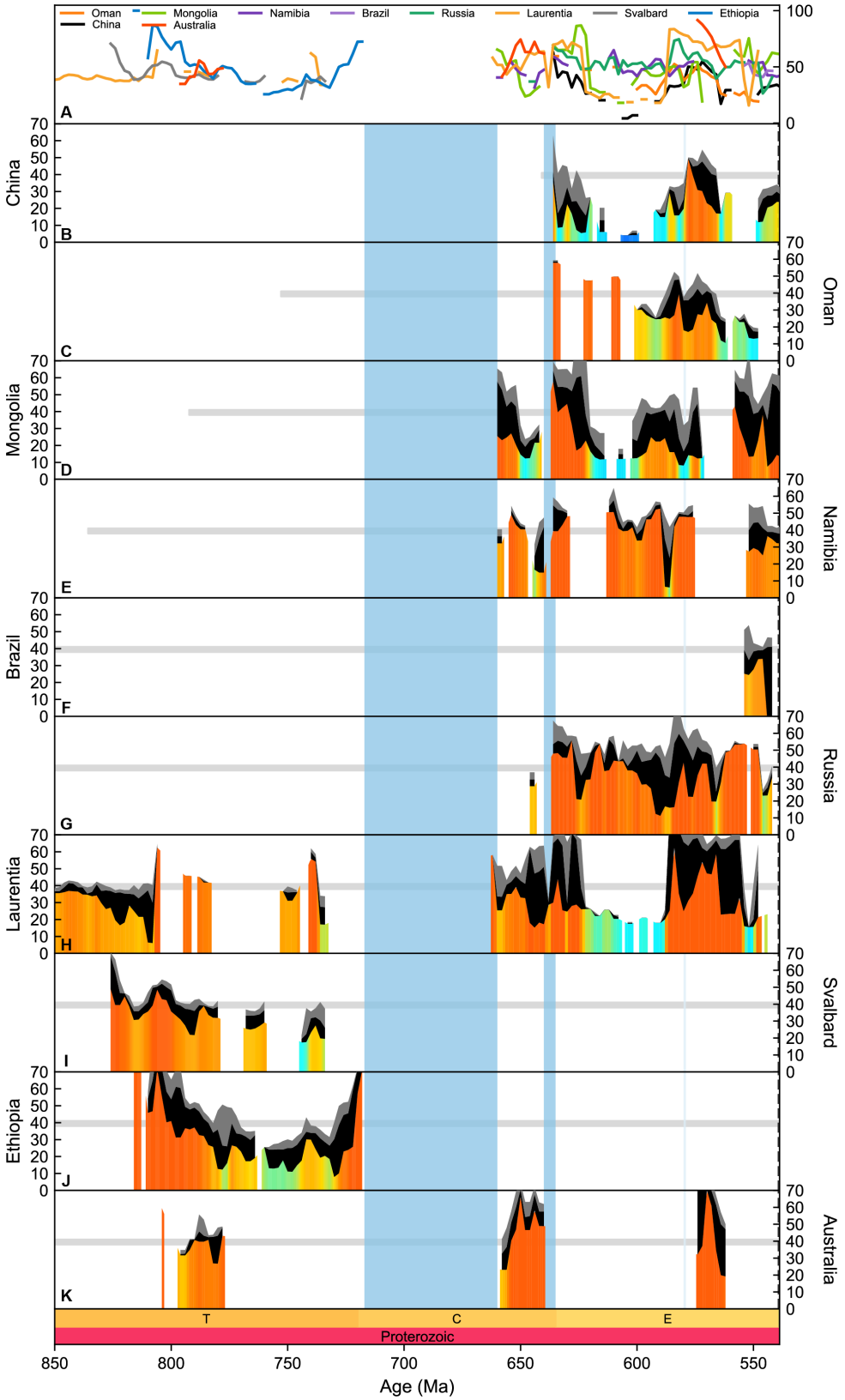
Oman
China
Mongolia
Australia
Namibia
Brazil
Russia
Laurentia
Svalbard
Ethiopia
A
B
C
D
E
F
G
H
I
J
K
China
Oman
Mongolia
Namibia
Brazil
Russia
Laurentia
Svalbard
Ethiopia
Australia
T
C
E
Proterozoic
850
800
750
700
650
600
550
Age (Ma)

Fig. S4. Neoproterozoic country-level contributions from only limestone included in Fig. 4C. (**A**) Temperature comparison of the different countries. (**B-K**) The 1^{st} to 25^{th} quantiles (black) and 25th to 50th quantiles (grey) of shallow marine temperatures from Scenario 1 estimated using quantile regression on points within 4 Myr windows sampled each 2 Myr. In panel order, data are plotted from China, Oman, Mongolia, Namibia, Brazil, Russia, Laurentia (USA and Canada), Svalbard, Ethiopia, and Australia. Grey bands represent the upper temperature limit of modern tropical subtidal ectotherms (*75*). Vertical bars indicate two Snowball Earth glaciations (dark blue) and one high latitude glaciation (light blue).

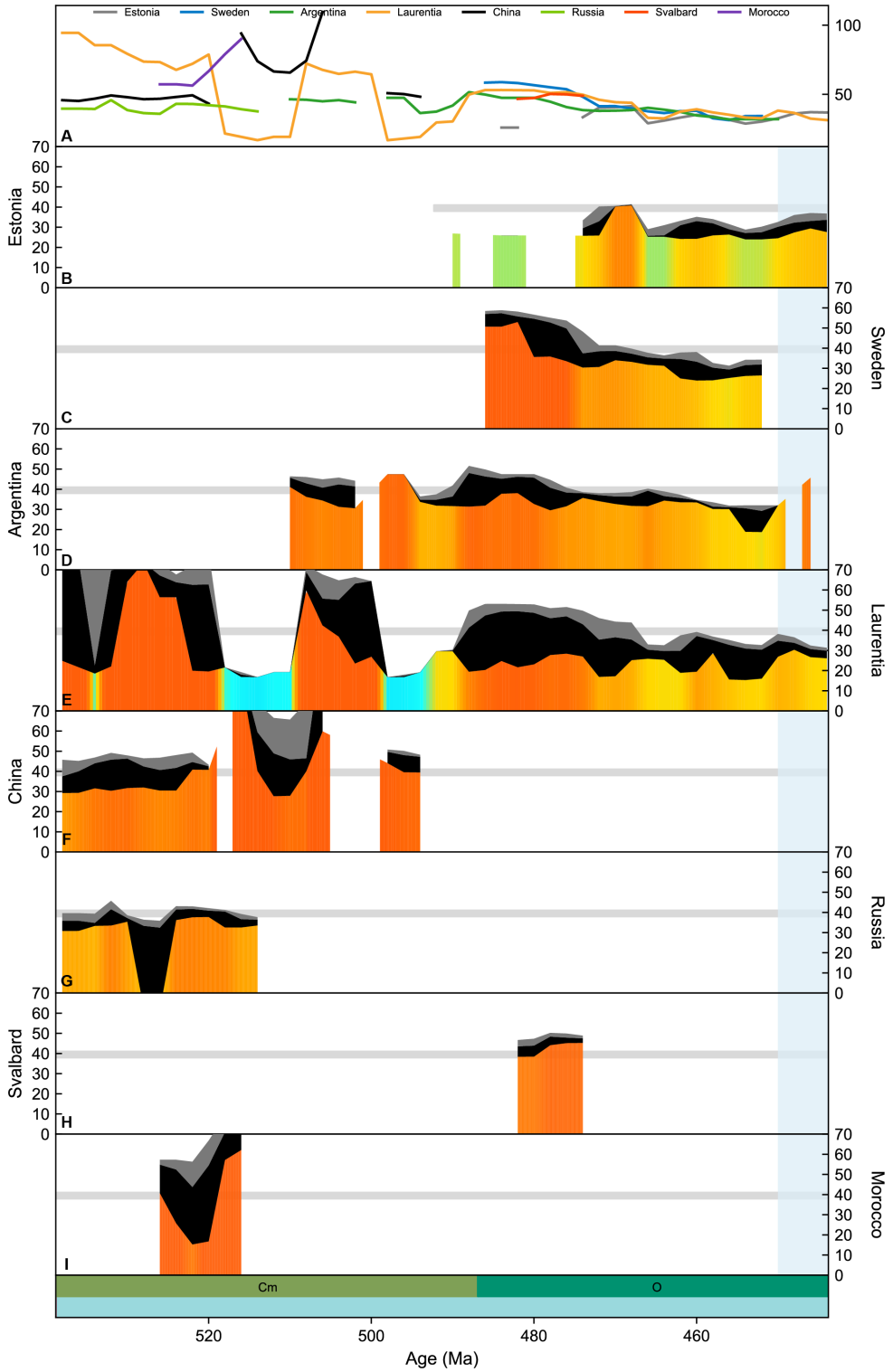

Fig. S5. Cambrian and Ordovician country-level contributions from limestone and fossils

included in Fig. 4C. (**A**) Temperature comparison of the different countries. (**B-I**) The 1^{st} to 25^{th} quantiles (black) and 25th to 50th quantiles (grey) of shallow marine temperatures from Scenario 1 estimated using quantile regression on points within 4 Myr windows sampled each 2 Myr. In panel order, data are plotted from Estonia, Sweden, Argentina, Laurentia, China, Oman, Russia, Svalbard, and Morocco. Grey bands represent the upper temperature limit of modern tropical subtidal ectotherms (*75*). Vertical bars indicate two Snowball Earth glaciations (dark blue) and one high latitude glaciation (light blue).

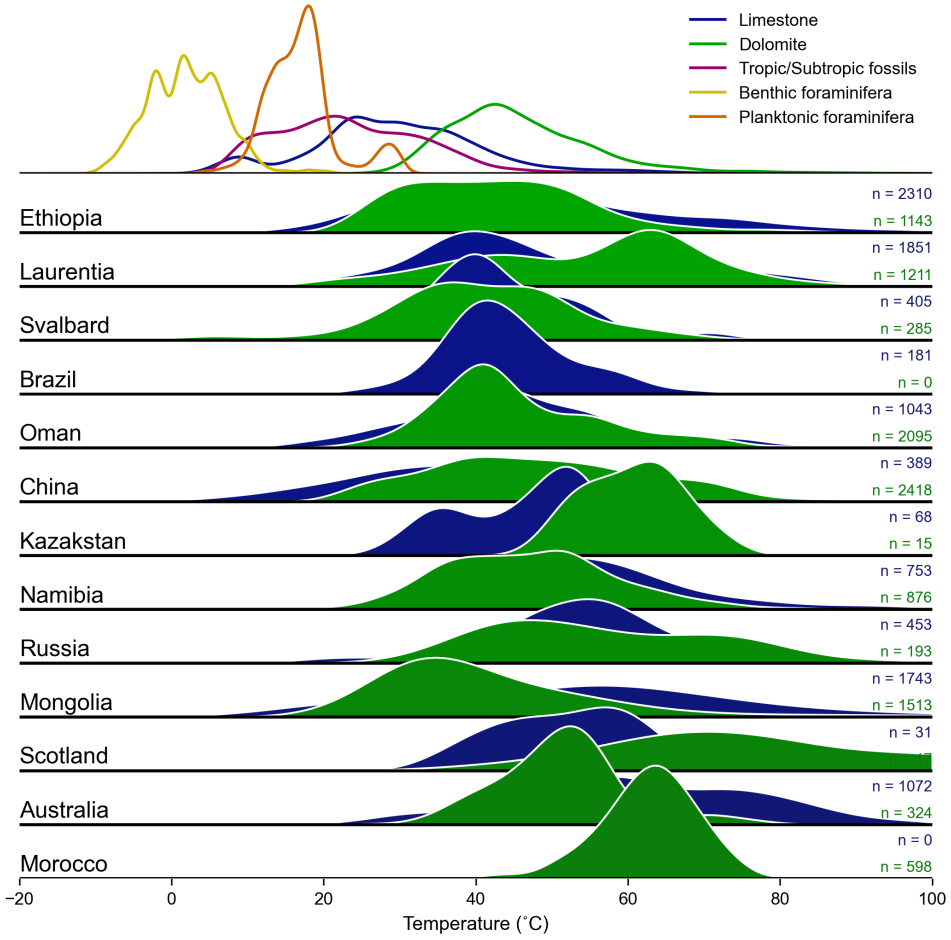

Fig. S6. Neoproterozoic Scenario 1 temperature distributions by location for limestone (blue) and dolomite (green) rocks compared to the post-Ordovician Phanerozoic distributions of limestone(blue), dolomite (green), coastal fossils (purple), planktonic foraminifera (orange), benthic foraminifera (yellow). Temperature distributions are generated on the unweighted points using Gaussian kernel density estimates as implemented in the scipy package in python with bandwidth selected using Scott's Rule. The number of points from each location are included to the right.

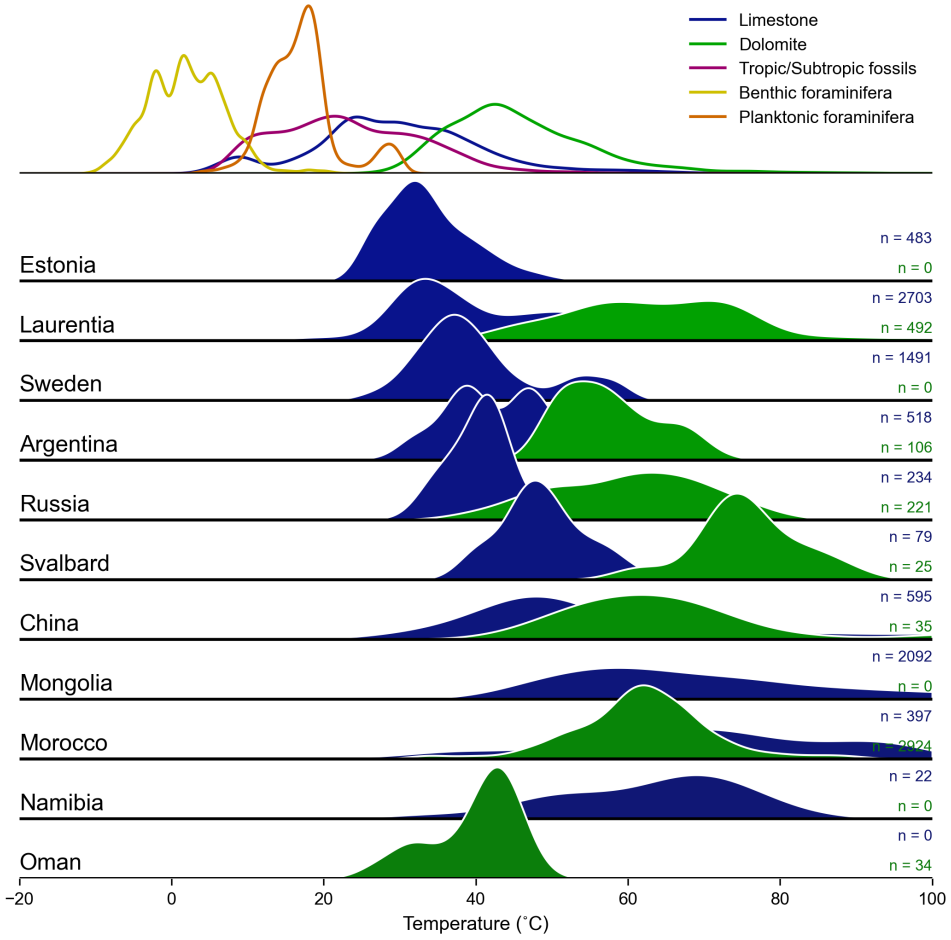

Fig. S7. Cambrian and Ordovician Scenario 1 temperature distributions by location for limestone (blue) and dolomite (green) rocks compared to the post-Ordovician Phanerozoic distributions of limestone(blue), dolomite (green), coastal fossils (purple), planktonic foraminifera (orange), benthic foraminifera (yellow). Temperature distributions are generated on the unweighted points using Gaussian kernel density estimates as implemented in the scipy package in python with bandwidth selected using Scott's Rule. The number of points from each location are included on the right.